Supporting Information

Mie Resonance Engineering in Meta-shell Supraparticles for Nanoscale Nonlinear Optics

Joong Hwan Bahng[1, ‡], Saman Jahani[1,‡], Douglas G. Montjoy[2], Timothy Yao[1], Nicholas Kotov[2], Alireza Marandi[1,*]

[1] Department of Electrical Engineering, California Institute of Technology, Pasadena, CA 91107, USA

[2] Department of Chemical Engineering, University of Michigan, Ann Arbor, MI 48109, USA

* email: marandi@caltech.edu

Keywords: colloids, nanostructures, metamaterials, nonlinear optics, Mie resonances

Table of Contents

1. Experiment – construction of meta-shell supraparticles (MSP)

1.1 Chemical synthesis of MSP

Comment 1: The colloidal meta-shell supraparticles (MSP) are constructed *via* aqueous colloidal synthesis under mild synthetic conditions. Initially, positively charged ZnO nanoparticles (NPs) (Sigma Aldrich) are electrostatically adsorbed onto negatively charged colloidal core spheres. The core spheres utilized for the construction of the MSP are polystyrene (PS) and silica (SiO_2) μ-spheres. We utilized carboxyl functionalized PS μ-spheres (Polysciences Inc.) that is imparted with interfacial negative charges. In order to impart interfacial negative charges to the SiO_2 μ-spheres, we overlaid the particle with polyelectrolyte Poly(allylamine hydrochloride) - Poly(acrylic acid) coating sequence in a layer-by-layer approach. The interfacial coating of ZnO NPs function as seeds from which ZnO nano-rods (NR) are grown in vertical orientations *via* a combination of hydrothermal and sonochemical processes. Synthetic methods to impart interfacial negative charges to the SiO_2 μ-spheres will be described in detail in the forthcoming publication "Photocatalytic Hedgehog Particles for High Ionic Strength Environments: Electric Field Catalysis without Electrodes".[1] In a typical synthesis that constructs the meta-shell of the MSP2.2 (1 μm in core dimeter, 600 nm in meta-shell thickness, total MSP diameter of 2.2 μm) , the ZnO NP coated core spheres are immersed in ZnO precursors, comprised of 25 mM of zinc nitrate hexahydrate ($Zn(NO_3)_2.6H_2O$, Sigma Aldrich) and 25 mM hexamethylenetetramine ($C_6H_{12}N_4$, Sigma Aldrich), dissolved in aqueous solution. ZnO NRs are grown by subjecting the mixture to hydrothermal (90^o) and sonochemical energy for 90 minutes. The length, thickness and the densities of the ZnO NRs in the meta-shell are easily tailored by adjusting their growth conditions, such as the growth time, ZnO pre-cursor concentrations and

the seeding density. The SiO_2 μ-spheres are synthesized by the well-known Stober process. The synthesized MSP are maintained as a dispersion in aqueous environment.

Comment 2: There are no synthetic restrictions to the choice of the core materials in constructing the MSP due to relaxation in the lattice-matching requirements for vertical orientation of 1D ZnO on any substrates.[2–4] The core sphere is an important design parameter as dielectric μ-sphere itself holds a wealth of EM modes.[5,6] Of particular interest is their collective interferences that lead to formation of a local $|E|$ hotspot at the shadow side of the particle upon light incidence, known as the photonic nanojet.[7,8] For an efficient SHG conversion, we want to maximize the spatial overlap of the $|E|$ hotspot with the interfacial array of $\chi^{(2)}$ ZnO NRs that constitutes the meta-shell. This requires the core refractive index to be $n < 2$.[7] Despite a polystyrene (PS) core best accomplishing the criteria (**SI 3.2, 3.3**), we focused our studies with the MSP having a SiO_2 core.

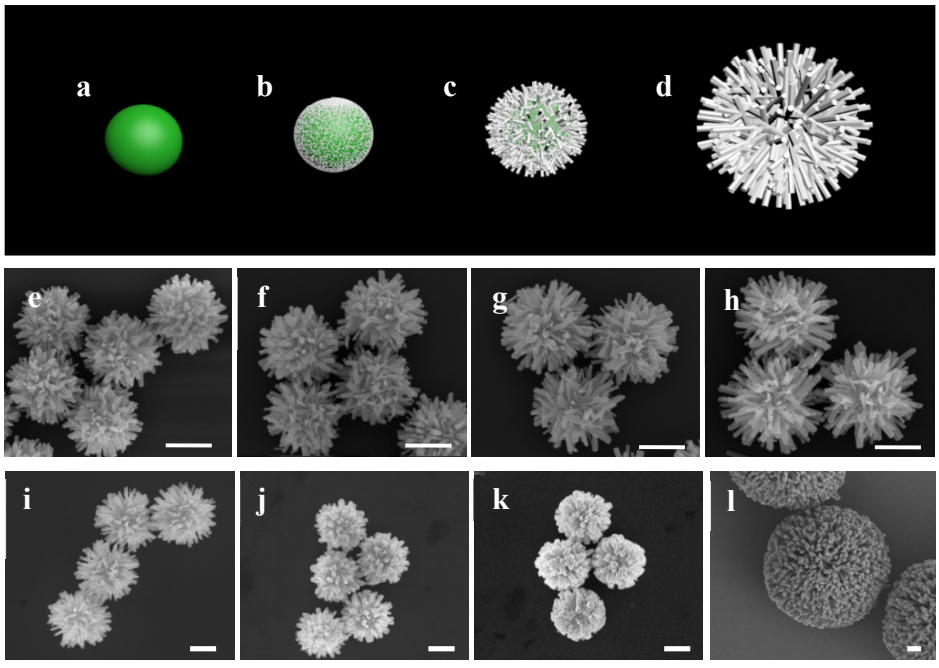

Figure S1. Meta-shell supraparticles. a-d, The MSP are synthesized by adsorbing positively charged ZnO NPs onto negatively charged dielectric μ-sphere, from which ZnO NRs are grown orthogonal to the sphere interface *via* a combination of hydrothermal and sonochemical processes; SEM images of the MSP with core particle of d = 1 μm and ZnO NRs of different lengths, **(e)** $l \approx 0.19$ μm, **(f)** $l \approx 0.27$ μm, **(g)** $l \approx 0.4$ μm, **(h)** $l \approx 0.6$ μm; SEM images of MSP with core particle of d = 1 μm and ZnO nanospikes of different widths, **(i)** $w \approx 0.19$ μm, **(j)** $w \approx 0.27$ μm, **(k)** $w \approx 0.4$ μm; (**l**) MSP with core particle d = 6 μm; scale bar = 1 μm

1.2 UV-Vis spectroscopy – extinction spectra of MSP

Comment: We first investigated light extinction spectra of the MSP as this provides us opportunity for an initial estimation and prediction of possible EM modes and their spectral locations supported by the supraparticle. The first series of the MSP were initially constructed with mono-disperse carboxyl functionalized polystyrene (PS) core spheres due to their commercial availability and due to simpler synthetic protocols in constructing the MSP. For studying optical nonlinear conversion by the MSP, the PS cores were subsequently replaced with SiO_2 core owing to its superior mechanical and thermal stability against high power laser. We first estimated the extinction characteristics of the MSP in their aqueous colloidal dispersion state. Two extinction peaks, atypical of low-index dielectric colloid for its representative size ranges, are observed. They are one broadband peak at ~ 730 nm (P_1) and another narrower peak at ~405nm (P_2), **Figure 2f** in the main text. For obtaining light extinction spectra in the aerosol format, lyophilized powder of MSP2.2 are placed in a quartz cuvette and suspended in mid-air *via* introduction of pressurized N_2 gas.

2. FDTD Simulations - extinction cross-section

2.1 Extinction cross-section of ZnO NRs and PS μ-spheres in aqueous dispersion

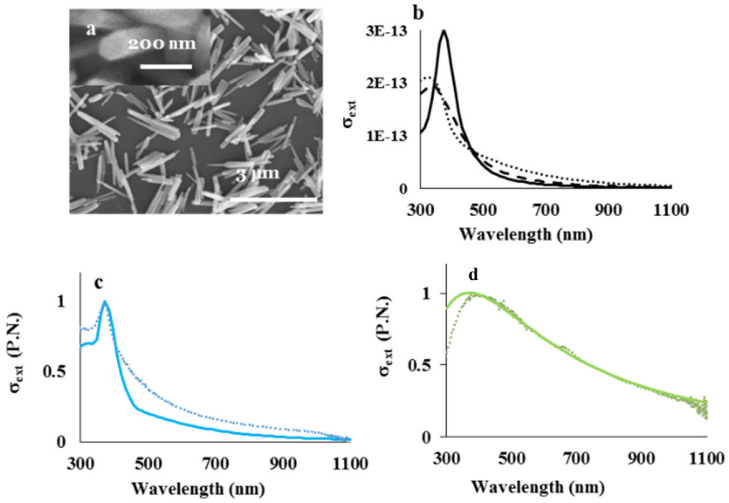

Figure S2. Extinction spectra of ZnO NR and PS μ-sphere, comparison between the spectroscopy and the FDTD simulation, in aqueous dispersion. (a) Scanning electron microscopy (SEM) image of independently synthesized ZnO NRs. The inset is a magnified view of the ZnO NRs in the meta-shell constructed on a core sphere that shows hexagonal cross-section. (**b**) FDTD simulation showing the extinction cross section (σ_{ext}) of a single ZnO NR (w = 120nm, l = 600nm) that is parallel to (solid line), at 45° angle to (dotted line) and perpendicular to (perforated line) the incident light; (**c**) FDTD simulation showing peak normalized extinction cross section (σ_{ext}, P.N.) of a single ZnO NR where the maximum extinction value per wavelength point are taken between the 3 incident angles (solid) *vs*. experimental the P.N. extinction of ZnO NRs measured with UV-Vis spectroscopy (dotted); (**d**) FDTD simulation showing the P.N σ_{ext} of a PS μ-sphere (solid), d = 1 μm, *vs*. the P.N. experimental extinction value from the spectroscopic measurement (dotted).

Comment: Lumerical FDTD Solutions are employed to characterize the optical properties of the colloidal particles. The finite difference time domain (FDTD) calculations of the extinction cross-section (σ_{ext}) of PS μ–spheres illuminated with total field scattered field (TFSF) plane wave source approximates the spectral line shape of the optical extinction from the spectroscopic measurement with good agreement. The FDTD simulations of the σ_{ext} of ZnO NRs also shows good agreement with the extinction measurement. A model ZnO NR is constructed to have length l = 600 nm, width w = 120 nm and a hexagonal cross-section. Larger discrepancy is due to polydispersity in the synthesized ZnO NRs.

2.2 Model MSP and its extinction cross-section in aqueous dispersion

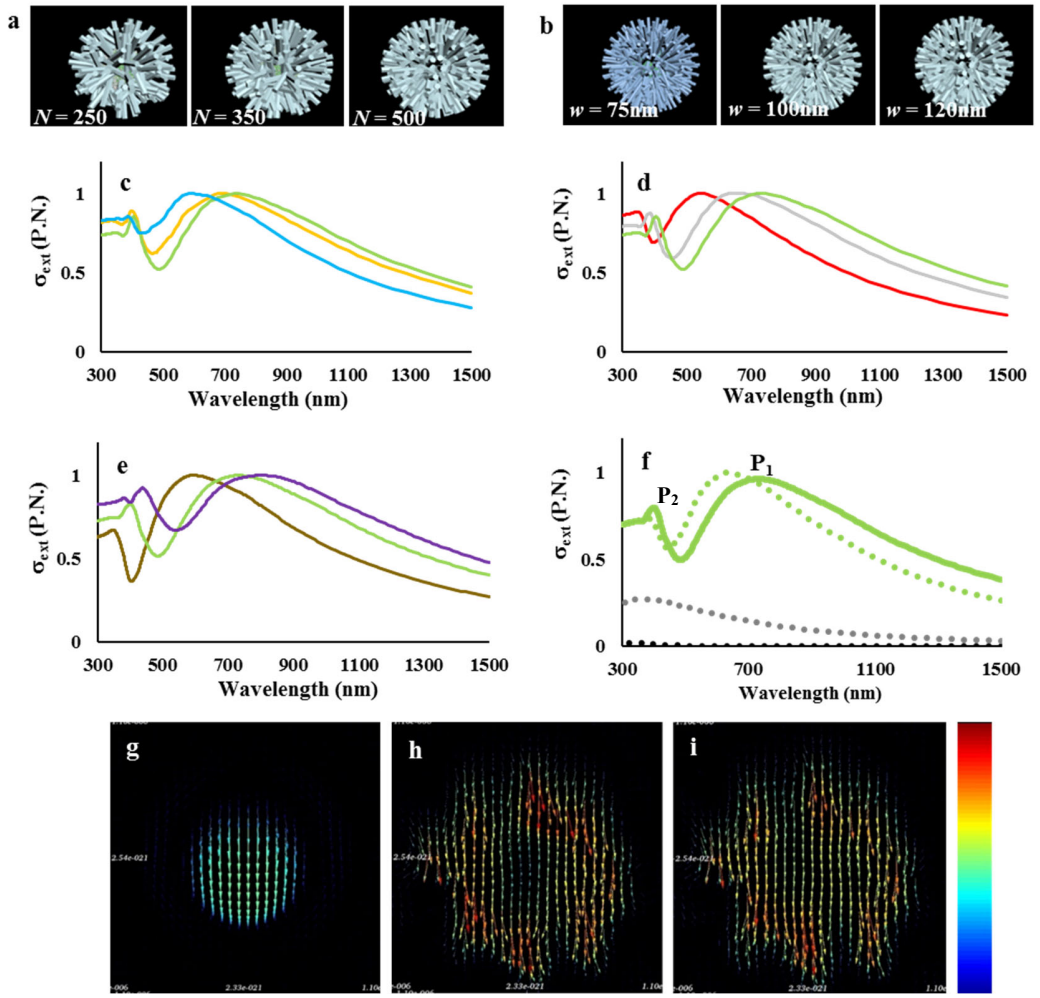

Figure S3. Model MSP and FDTD simulations. a-b, Model MSP is constructed, *via* computer aided design (CAD) software, by layering ZnO nanoparticles (pyramids, 15 nm) on SiO_2 or PS μ-sphere, onto which vertically oriented ZnO NRs are scattered to create imperfect orthogonalization that reflect the experimental construct. The model MSP are imported into the FDTD simulations; the CAD of model MSP with meta-shell having varying ZnO NR (**a**) densities and (**b**) thicknesses. **c-f**, FDTD simulations showing the P.N. σ_{ex} of the MSP having (**c**) variations in the ZnO NR densities N (constant l = 600 nm and w = 120 nm) with N = 500 (green), N = 350 (orange), N = 250 (blue) and (**d**) variations in the ZnO NR width w (constant l = 600 nm and N = 500) with w = 120 nm (green), w = 100 nm (grey), w = 75 nm (red) and (**e**) variations in the ZnO NR length l (constant w = 120 nm and N = 500) with l = 300 nm (brown) where l = 600 nm (green), l = 900 nm (purple); (**f**) evolution of σ_{ext} starting from single ZnO NR (black, dotted), PS μ-sphere (grey, dotted) to meta-shell only (spherical array of ZnO NRs, N = 500, l = 120 nm, w = 120 nm, green, dotted) to the MSP (green, solid); **g-i**, FDTD simulations, at incident λ = 730 nm, displaying electric field profile at the center cross-section of a (**g**) PS μ-sphere (d = 1 μm), (**h**) meta-shell only and (**i**) the MSP. All FDTD simulations carried out here is modeled as aqueous dispersion of MSP to emulate UV-Vis spectroscopic measurement procedure.

Comment: FDTD simulations are employed to characterize the optical linear properties of the MSP. We created a model MSP composed of either a SiO_2 or a PS core of diameter d = 1 μm and the meta-shell consisting a spherical array of ZnO NRs (length l = 600 nm, thickness w = 120 nm) that mirrors the experimental construct. Computer aided design software was used to reconstruct a model MSP with imperfect orthogonalization of ZnO NRs to mirror the experimental construct and to remove artifacts due to symmetry that is not present in the experimental construct (**Figure S3a, b**). The FDTD full wave simulations of the σ_{ext} by the model MSP2.2 subject to TFSF source approximates the experimental extinction line shape from the UV-Vis spectroscopy measurement with good agreement, **Figure 2j** in the main text. The simulation also recaptures the ZnO NR density-, width-, and length-dependent spectral redshift in the extinction peaks, **Figure S3c-e**.

The lack of spectral correlation between the MSP and its components, the ZnO NR and the core sphere (**Figure S2**), suggest that the peak P_1 originate from the supraparticle architecture. Indeed, the evolution of the σ_{ext} from a ZnO NR, PS μ-sphere, meta-shell only and to the model MSP shows that the ortho-spherical arrangement of the ZnO NR array, that constitutes the meta-shell, is the governing structural attribute that generates the broadband peak, **Figure S3f**. The broadband peak further redshifts to P_1 in the presence of the core sphere. This is due to increase in the electric polarizability that extends the electric field profile through the core substrate, **Figure S3g-i**.

2.3 Simplified triple-shell core model and its extinction cross-section in aqueous dispersion

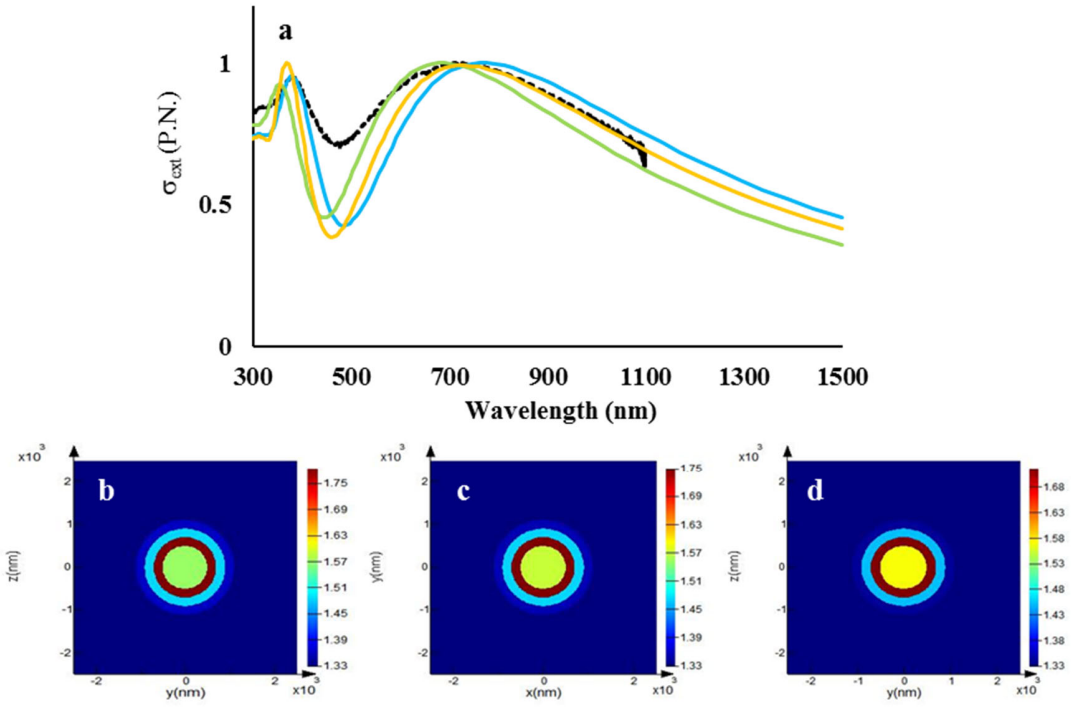

Figure S4. Discretized gradient refractive index triple-shell model; triple-shell model having 1:1:1 thickness ratios with graded variations in the refractive indices, where the refractive index of each shell layers are determined by Maxwell Garnett effective medium approximations; (**a**) FDTD simulations of the P.N. σ_{ext} of the triple-shell model that corresponds to MSP having ZnO NR of w = 120 nm, l = 600 nm and N = 275 (**blue**), N = 265 (**orange**), N = 250 (**green**). The perforated black line represents the spectroscopic measurement (A.U.) of MSP in aqueous suspension. Color map of the refractive indices in the 1:1:1 triple-shell that corresponds to (**b**) N = 275 (f_{outer} = 0.27 , f_{middle} = 0.42, f_{inner} = 0.75), (**c**) N = 275 (f_{outer} = 0.26 , f_{middle} = 0.41, f_{inner} = 0.72), (**d**) N = 250 (f_{outer} = 0.25 , f_{middle} = 0.39, f_{inner} = 0.68), where f is the volume fraction of ZnO.

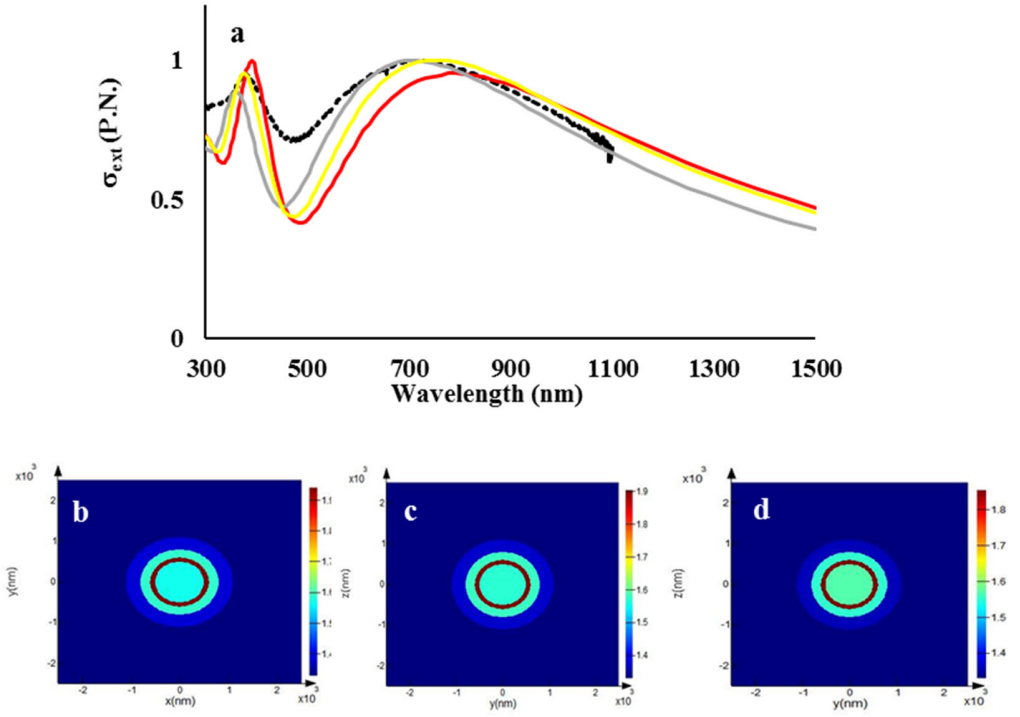

Figure S5. Discretized gradient refractive index triple-shell model. triple-shell model having 3:2:1 (outer:middle:inner) thickness ratios with graded variations in the refractive indices, where the refractive index of each shell layers are determined by Maxwell Garnett effective medium theory; (**a**) FDTD simulations of the P.N. σ_{ext} of the triple-shell model that corresponds to the MSP having ZnO NR of w = 120 m, l = 600 nm and N = 275 (**red**), N = 265 (**yellow**), N = 250 (**grey**). The perforated black line represents the spectroscopic measurement of the MSP in aqueous suspension. . Color map of the refractive indices in the 3:2:1 triple-shell that corresponds to (**b**) N = 275 (f_{outer} = 0.3 , f_{middle} = 0.55, f_{inner} = 0.90), (**c**) N = 265 (f_{outer} = 0.29 , f_{middle} = 0.53, f_{inner} = 0.87), (**d**) N = 250 (f_{outer} = 0.27 , f_{middle} = 0.50, f_{inner} = 0.82),), where f is the volume fraction of the ZnO.

Comment: It should be noted that the model MSP2.2 requires higher nanospike densities (N) to match the σ_{ext} spectra of the FDTD calculations with the spectroscopic measurement from the experimental construct ($N_{experiment}$~$200 - 250$, $N_{model} = 500$). This may be due to large unit mesh size applied in the calculation so as to remain within the computational budget. Such may not grasp the geometrical finesse and complexities within the meta-shell. On the other hand, simplifying the empirical meta-shell features into a simplified core-shell model should yield

extinction line shape with good agreement between the simulation and the spectroscopic measurements. Due to vertical orientation of high aspect-ratio ZnO NR in a spherical format, the meta-shell is represented with radial graded refractive index profile with 3 discretized shells at 1:1:1 or 3:2:1 (outer: middle: inner shell) thickness ratios, layered on the core sphere. Refractive indices, *n*, of each shells are assigned by the effective medium approximation (EMA) using Maxwell Garnett mixing rule for two-phase heterogeneous media.[9,10] The FDTD calculations of the σ_{ext} of the triple-shell model with $N_{3-shell} = 250 \sim 275$, which is a close representation of the experimental MSP2.2, indeed shows good agreement with the experimental measurement, **Figure S4, S5**.

2.4 Model MSP and its extinction cross-section in air

Comment: In carrying out the FDTD simulations to probe the optical properties of the MSP2.2 in an aqueous environment, the model MSP2.2 required ZnO NR density of $N = 500$ to achieve a good match with the spectroscopic measurements (**Section 2.2**). Interestingly, in carrying out the FDTD simulations of the σ_{ext} with the model MSP2.2 in air, the ZnO NR density of $N = 300$ was sufficient to yield good match with the experiment. This may be due to higher visibility of the surface corrugation within the meta-shell owing to higher index contrast. The latter model MSP2.2 *(*with $N = 300$) is a closer representation to the empirical observations in the experimental construct ($N = 200 – 250$). There is a good agreement in the extinction lineshape between the FDTD simulations and the experimental spectroscopic measurement (**Figure 2k**, main text).

3 FDTD Simulations – Photonic nanojet in *MSP*

3.1 Engineering photonic nanojet with meta-shell

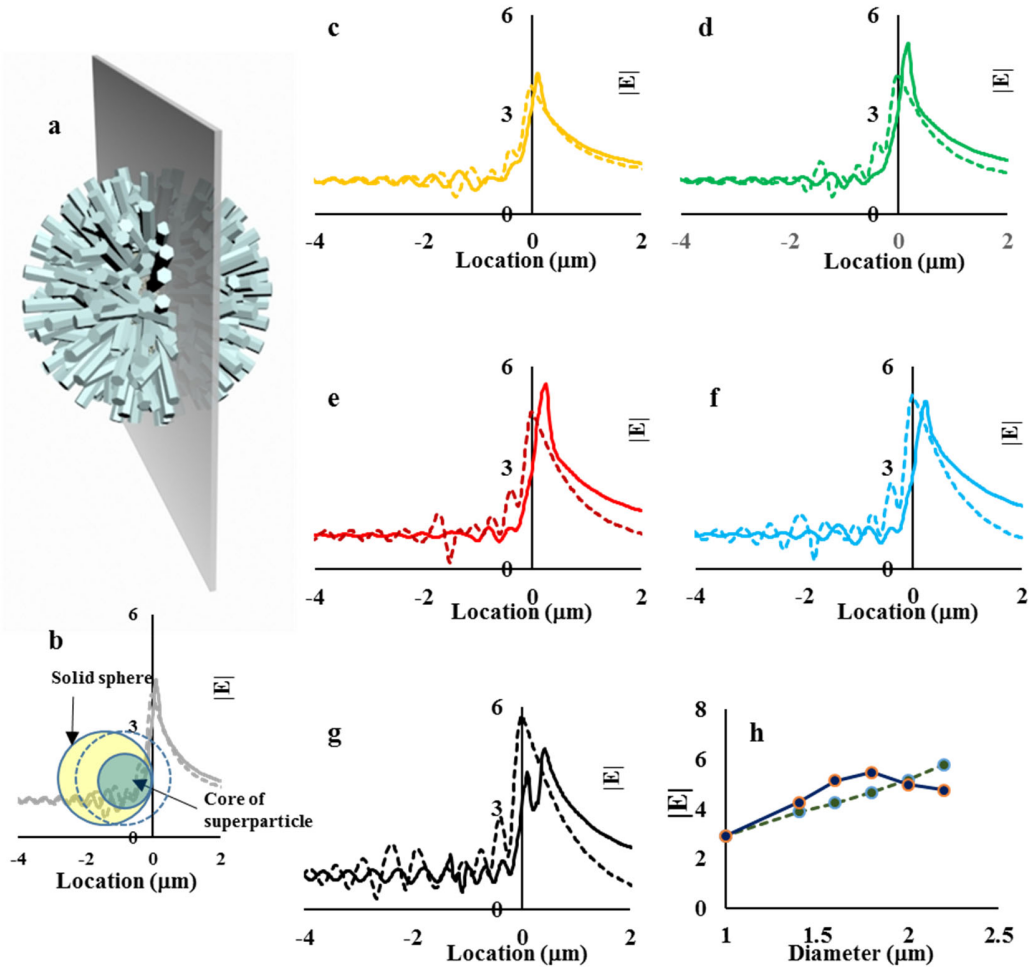

Figure S6. Effect of meta-shell thickness on the photonic nanojet generated by the MSP. Comparison of the electric field strength |E| in the photonic nanojet formed by the MSP and that formed by a solid sphere of equivalent diameter to the MSP. The refractive index of the solid sphere in comparison is the same as that of the core in the MSP. FDTD simulation is carried out at incident $\lambda = 900$ nm and the |E| profile is plotted along the (**a**) middle cross-section of the MSP (or solid sphere). The thickness of the MSP is varied while the SiO_2 core diameter is kept constant at 1 μm. (**b**) $x = 0$ coordinately coincides at the interface between the meta-shell and the core in the MSP and at the solids sphere interface (yellow), both at their shadow side; **c-g**, comparison of |E| in the photonic nanojet formed by MSP (solid) and that by the solid SiO_2 sphere (perforated) of equivalent diameters, (**c**) $d = 1.4$ μm, (**d**) $d = 1.6$ μm, (**e**) $d = 1.8$ μm, (**f**) $d = 2$ μm, (**g**) $d = 2.2$ μm; (**h**) peak |E| along the middle cross-section of the photonic nanojets formed by the MSP (solid) and by the SiO_2 solid spheres of equivalent diameters (perforated).

Comment: In this section, we employed FDTD simulation to observe the effect of the meta-shell thickness on the photonic nanojet features generated by the MSP. The core refractive index and its diameter are kept constant (SiO_2, d = 1 μm), while the thickness of the meta-shell is varied. The photonic nanojet features observed in the MSP are also compared with that formed by a solid SiO_2 sphere with equivalent overall diameter to the MSP. In the graphs in **Figure S6c-g**, x = 0 coordinately coincides at the interface between the core and the meta-shell in the MSP at its shadow side, **Figure S6b**. The x = 0 also coordinately coincides at the interface of the solid SiO_2 sphere at its shadow side.

In **Figure S6h,** d = 1 μm represents the bare core sphere (MSP without meta-shell). Compared to a bare SiO_2 core sphere, peak electric field strength |E| in the photonic nanojet is always higher in the presence of a meta-shell.

When the overall diameter d < 2 μm, the peak |E| in the photonic nanojet is higher in the MSP than that produced by the SiO_2 solid sphere of equivalent diameter to the MSP, **Figure S6c-e**. When d > 2 μm the trend reverses, **Figure S6f, g**. This is due to scarcity in the ZnO NR density at the peripheral edges, with increasing meta-shell thickness, which weakens its effective size. It can also be seen that the spatial location of the peak |E| in the photonic nanojet hotspot proceeds away from the core interface with increasing meta-shell thickness. Meanwhile, the photonic nanojet hotspot remain fixed at the interface for the SiO_2 solid sphere, despite variations in their sizes.

3.2 Stronger $|E|$ hotspot in the photonic nanojet in the presence of a meta-shell

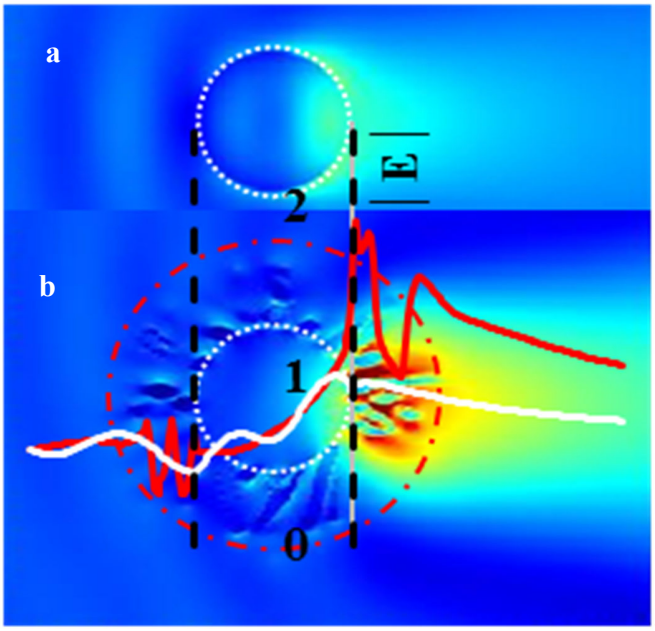

Figure S7. FDTD simulation showing stronger $|E|$ in the photonic nanojet hotspot in the presence of a meta-shell. Full wave FDTD simulation that compares the peak $|E|$ in the photonic nanojet hotspot generated by a (**a**) SiO_2 core sphere alone (white) and that by (**b**) the model MSP2.2 (red). (**a**) In the case of the bare core sphere, the region of peak $|E|$ is confined within the core sphere, (**b**) In the case of the MSP, the region of peak $|E|$ is localized in the meta-shell comprised of the $\chi^{(2)}$ nanostructures. The diameter of the core sphere is $d = 1$ μm, thickness of the meta-shell is 600 nm. The permittivity of the sphere is $\varepsilon = 2.2$. The input wavelength is $\lambda = 1550$ nm.

3.3 Influence of core refractive index on the photonic nanojet profile

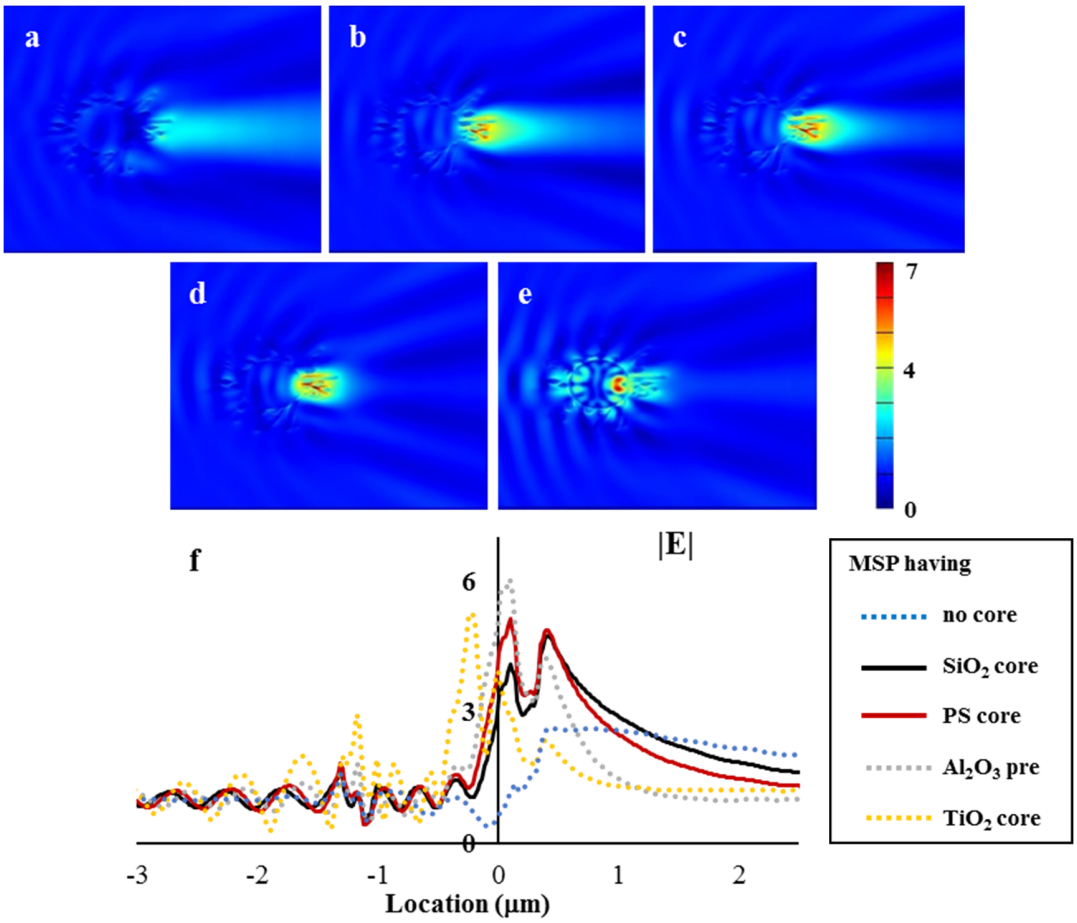

Figure S8. Effect of the refractive index *n* of the core sphere in the MSP on the photonic nanojet. FDTD full wave simulation displaying electric field profile at the middle cross-section of the photonic nanojet formed by the MSP having (**a**) no core and (**b**) SiO_2 (n = 1.47), (**c**) PS (n = 1.57), (**d**) Al2O_3 (n = 176), (**e**) TiO_2 (n = 2.5) core sphere (d = 1 µm). Increase in the refractive index n of the core sphere increases the peak |E|, but also shifts the hotspot volume towards the center of the particle. For TiO_2 core, the region of peak |E| is confined near the interface but concentrated within the core sphere. (**f**) Electric field strength |E| long the middle cross-section of the MSP having no core (blue dotted), SiO_2 core (black), PS core (red), Al_2O_3 core (grey dotted) and TiO_2 core (orange dotted).

Comment: Here, we investigated changes in the photonic nanojet features with variations in the core refractive index n. The geometrical features and materials properties of the meta-shell is

kept constant. Increase in *n* increases the peak electric field strength |E| in the photonic nanojet formed by MSP. This is due to higher mode densities supported by the higher index dielectric spheres whose collective interference yields higher |E|. Furthermore, increase in *n* causes migration of the photonic nanojet hotspot towards the core interface. At sufficiently high *n* (≥2), the photonic nanojet diminishes and the hotspots are dispersed within the core sphere. This is an unsuitable feature for optical nonlinear generations with the MSP as most of the input power does not overlap with the $\chi^{(2)}$ nanostructures. Ideally, core sphere should be chosen such that the MSP generate the hotspot whose mode volume maximizes the $\chi^{(2)}$ nanostructure coverage and whose |E| maximum intensity coincides with the spatial location of highest $\chi^{(2)}$ nanostructure densities. Despite the PS core best describing the aforementioned condition, we have chosen the SiO_2 core for our studies due to its higher stability against high power laser pulses.

4. Analytical Calculations

4.1 Modeling

The average unit-cell size of the nanowires at the outer interface of the particle is sub-wavelength. Hence, we can approximate the nanowires using an effective medium approach. Since the nanowires are mostly oriented radially, we can model them with all-dielectric radial anisotropy using Maxwell-Garnett approximation. The effective permittivity parallel and normal to the direction of the nanowires are:[11]

$$\varepsilon_{\perp} = \rho(r)\varepsilon_d + \big(1 - \rho(r)\big)\varepsilon_h,$$

$$\varepsilon_{\parallel} = \frac{\big(1+\rho(r)\big)\varepsilon_d\varepsilon_h + \big(1-\rho(r)\big){\varepsilon_h}^2}{\big(1-\rho(r)\big)\varepsilon_d + \big(1+\rho(r)\big)\varepsilon_h}$$

where ε_d is the permittivity of the dielectric nanowire, ε_h is the permittivity of the host medium (which is air here), and $\rho(r)$ is the nanowire filling factor. Since the density of the nanowires reduces as the distance from the center increases, the filling factor is *r*-dependent. This results in a graded-index profile in the shell. For the TE (magnetic) modes, the electric field in the *r* direction is zero. Hence, the TE modes do not feel the anisotropy of the shell. However, the TM (electric) modes are affected by the anisotropy of the shell.

To calculate the scattered fields, we have used the Mie theory. We have assumed the input is a plane wave polarized in the *x* direction and propagates in the *z* direction. The input electric field intensity is E_0. The electric and magnetic fields of TE and TM modes in the *r* direction in the mth-medium can be written as:[12]

$${E_r}^m(r,\theta,\varphi) = \frac{E_0}{k_0^2 r^2}\cos\varphi \sum_n i^{(n+1)}(2n+1)a_n^m\, z_{n_{e,m}}\big(k_0\sqrt{\varepsilon_{\perp,m}}r\big)P_n^{(1)}(\cos\theta),$$

$${H_r}^m(r,\theta,\varphi) = \frac{E_0}{Z_0 k_0^2 r^2}\cos\varphi \sum_n i^{(n+1)}(2n+1)b_n^m\, z_n\big(k_0\sqrt{\varepsilon_{\perp,m}}r\big)P_n^{(1)}(\cos\theta),$$

where $z_n(x)$ is a spherical Bessel function of nth-order, $P_n^{(1)}$ is associate Legendre function of 1st order and nth degree, $\varepsilon_{\perp,m}$ is the effective transverse permittivity of the mth-medium, and η is the impedance of the frees-pace. The order of the Bessel functions in anisotropic media is:

$$n_{e,m} = \sqrt{\frac{\varepsilon_{\perp,m}}{\varepsilon_{\parallel,m}} n(n+1) + \frac{1}{4}} - \frac{1}{2}.$$

It is seen that by changing the anisotropy, we can control the index of the Bessel function for the electric modes.

To model the graded-index profile, we have discretized the metamaterial shell to 40 homogenous layers. By applying the boundary conditions at the interface between each layer, we can find the scattering coefficients of the particle with metamaterial shell

4.2 Scattering coefficients of electric and magnetic multipoles in the core and in meta-shell

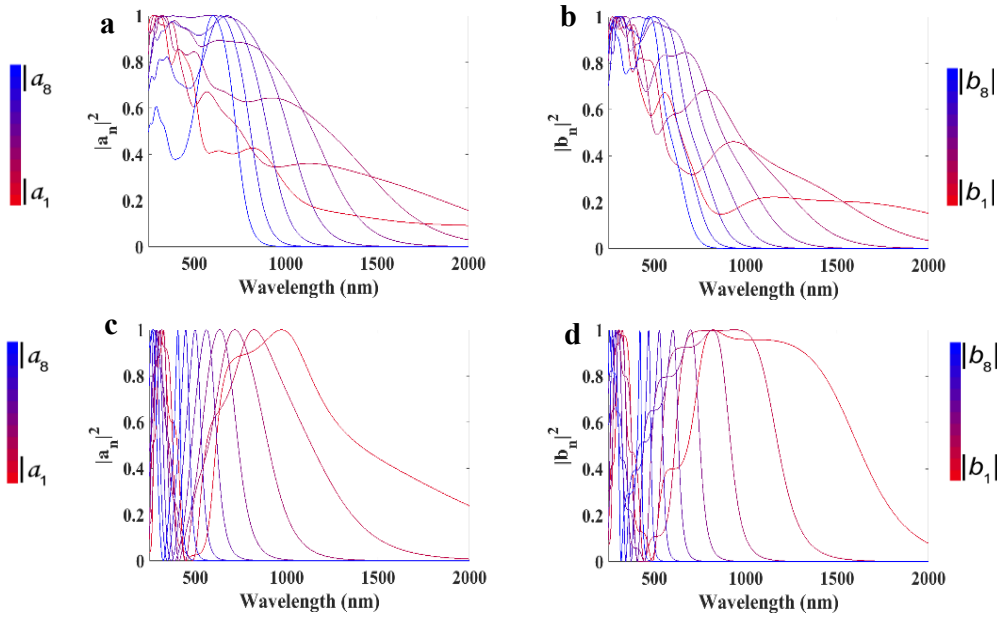

Figure S9. Scattering coefficients of electric and magnetic multipoles in the core sphere and in the meta-shell. Scattering coefficients of (**a**) electric mode and (**b**) magnetic mode in the meta-shell, (**c**) electric mode and (**d**) magnetic mode in the SiO2 core μ-sphere, d = 1 μm.

4.3 Mie resonance engineering with radial graded index and spherical anisotropy

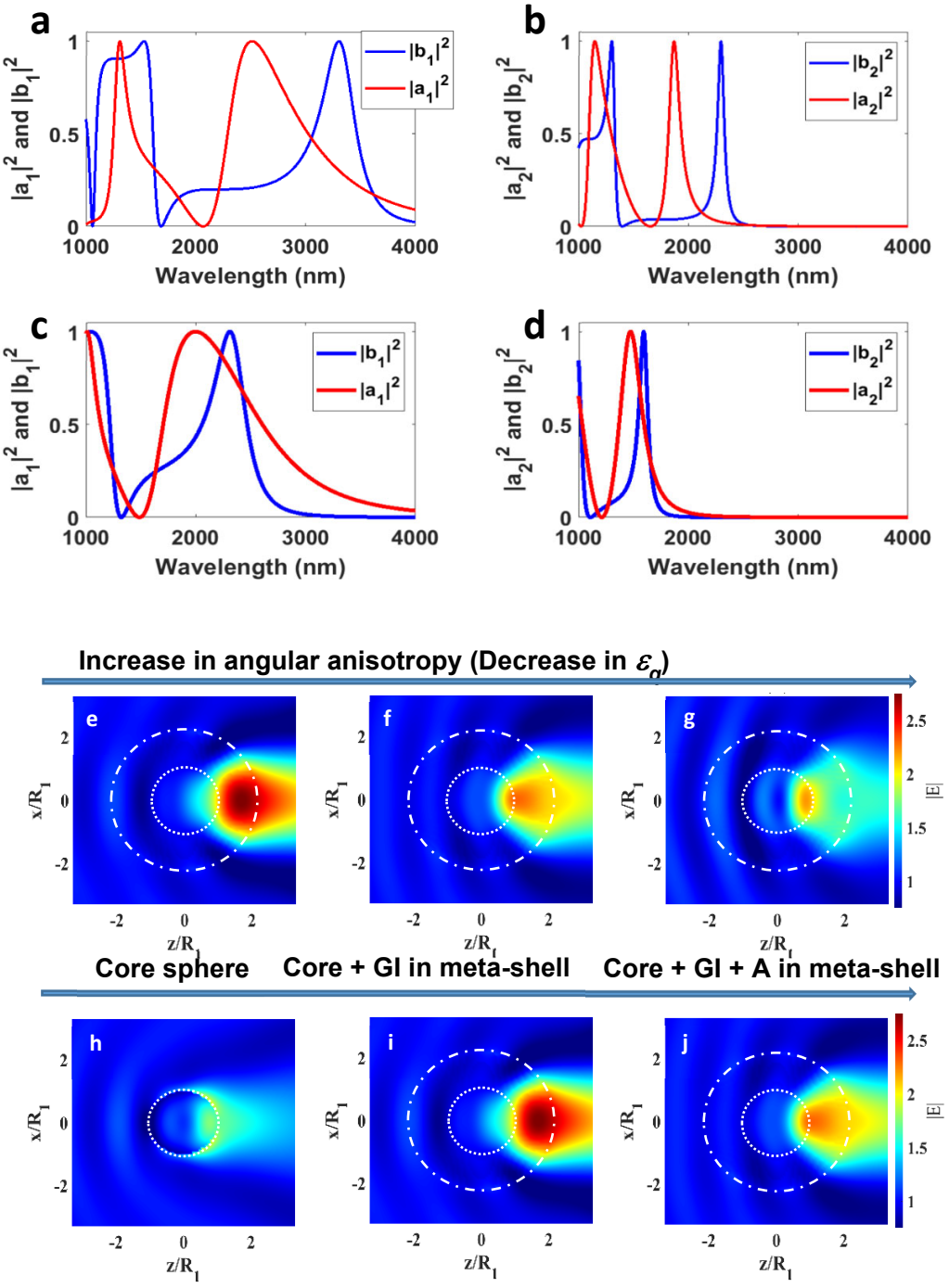

Figure S10. Mie resonance engineering the meta-shell. The diameter of the core sphere is d_{core} = 1 mm, thickness of the meta-shell is t_{shell} = 600 nm. The permittivity of the sphere is e_{core} = 2.2; **a-d**, Increase in the radial graded index increases the spectral overlap between the electric and magnetic modes. Scattering coefficients of **a**) ED and MD, **b**) EQ and MQ for an isotropic sphere of d = 1.4 μm, ε = 10. Scattering coefficients of **c**) ED and MD, **d**) EQ and MQ for a core shell model ascribed with graded index profile in the shell. Here, core d = 1 μm, ε = 10 and shell d = 0.4 μm and ε radially decrease from 10 (core) to 1 (shell outer peripheries); **e-g**, increase in the anisotropy shifts the hotspot towards the core sphere interface, (**e**) $e_{q,\ shell}$: 2.2, (**f**) $e_{q,\ shell}$: 1.5, (**g**) $e_{q,\ shell}$: 1; Here, the radial anisotropy is kept constant, $e_{r,\ shell}$ = 2.2. The input wavelength is λ = 1550 nm (the input wavelength is λ = 900 nm for identical plots in the main text, **Figure 4**); **h-j**, matching the analytical parameters to empirical measurements, photonic nanojet features are reproduced for (**h**) the core sphere and (**j**) the model MSP2.2 observed in the FDTD full wave simulation (**SI 3.2**); (**i**) While the peak $|E|$ is higher without the spherical anisotropy in the meta-shell, the region of peak $|E|$ shift towards, but exterior to, the core interface, at which the density of the $\chi^{(2)}$ nanostructures are at its highest.

Comment: This section shows further example of how increase in the radial gradient index helps with the spectral overlap of electric and magnetic modes. Compared to an isotropic sphere (d = 1.4 μm, ε = 10), there is significant increase in the spectral overlap between the electric and magnetic modes for the core-shell model (d = 1 μm, ε = 10) in which the shell is ascribed with graded index profile (d = 0.4 μm, ε = 10 -> 1). **Figure S10a** shows scattering coefficients of ED and MD and **S10b** shows scattering coefficients of EQ and MQ for the isotropic sphere. **Figure S10c** shows scattering coefficients of ED and MD and **Figure S10d** shows scattering coefficients of EQ and MQ for core-shell model with graded index in the shell.

5. FDTD simulations – Nonlinear optics with MSP

5.1 Normalized conversion efficiency η_{SHG} (W^{-1}) calculations

Comment: In running the full wave FDTD (Lumerical FDTD Solutions) calculations for second harmonic processes, the collection wavelengths $\lambda_{2\omega}$ is set to the second harmonic ranges and the simulation is carried out in a "nonorm" state. This removes numerical artifacts associated with the continuous wave approximation/normalization from the input pulse, λ_{ω}, whose pulse length τ_{ω} does not expand to the collection wavelength $\lambda_{2\omega}$. The output power, $\widetilde{P_{2\omega}}$, collected from the frequency domain field and power monitor is separately renormalized with the output pulse length $\tau_{2\omega}$, to obtain $P_{2\omega}$. The input power, $\widetilde{P_{\omega}}$, collected from the frequency domain monitor is renormalized with the pulse length τ_{ω}. This represents the peak power, P_{ω} , delivered to the model MSP.

$$P_{2\omega} = \frac{\widetilde{P_{2\omega}}}{{\tau_{2\omega}}^2}$$

$$P_{\omega} = \frac{\widetilde{P_{\omega}}}{{\tau_{\omega}}^2}$$

The normalized SHG conversion efficiency, η_{SHG}, is obtained by dividing the output power by the input power squared.

$$\eta_{SHG} = \frac{P_{2\omega}}{{P_{\omega}}^2} = \frac{\widetilde{P_{2\omega}}}{\widetilde{P_{\omega}}^2} \times \frac{{\tau_{\omega}}^4}{{\tau_{2\omega}}^2}$$

5.2 Effect of core refractive index on the SHG conversion efficiency

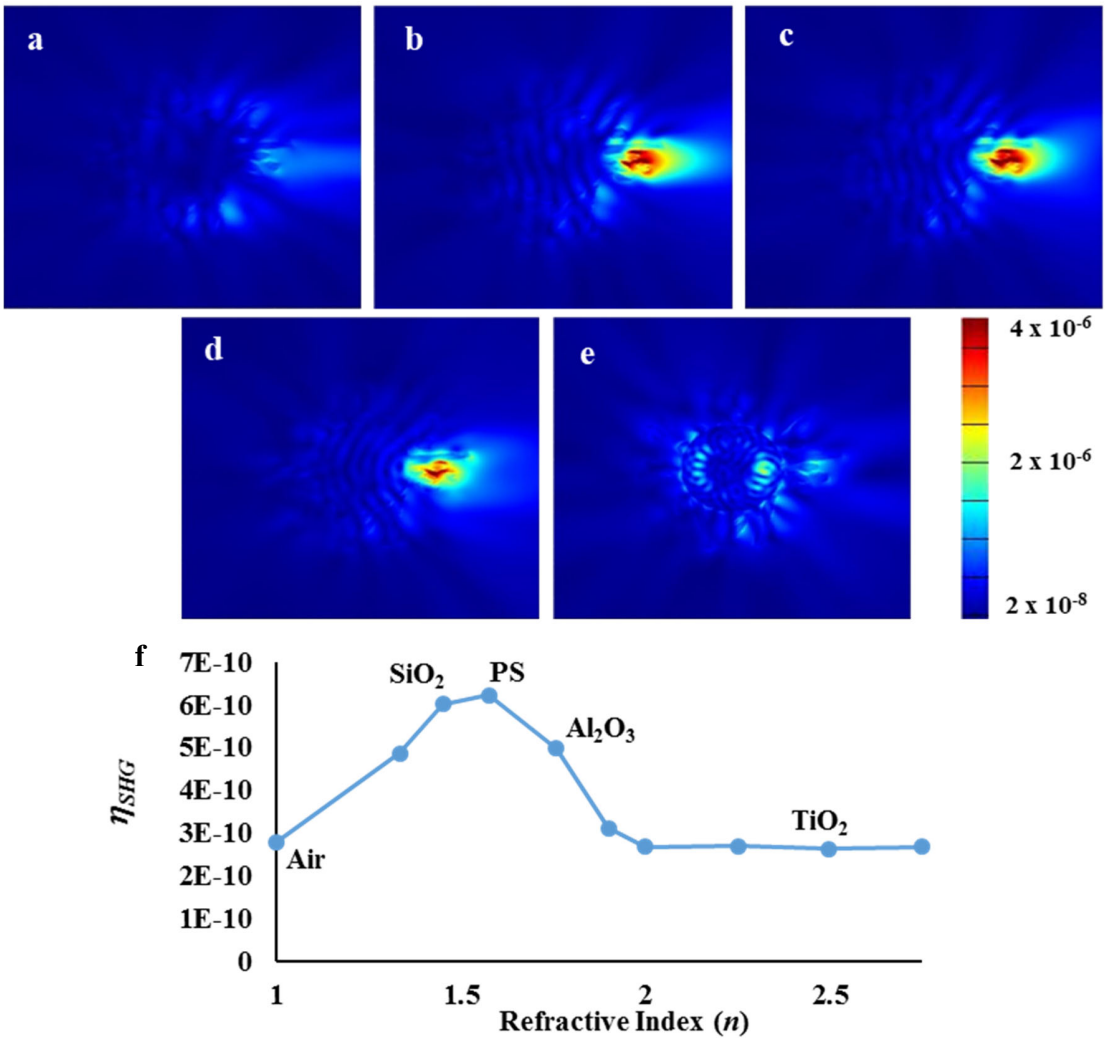

Figure S11. Influence of core refractive index *n* on the SHG conversion efficiency η_{SHG} of the MSP. FDTD full wave simulation displaying the middle cross-sectional electric field profile, |E|, of the SHG generated by the MSP having (**a**) no core and (**b**) SiO_2 (n = 1.47), (**c**) PS (n = 1.57), (**d**) $Al2O_3$ (n = 176), (**e**) TiO_2 (n = 2.5) core sphere (d = 1 μm). The thickness of the meta-shell is 600 nm. (**f**) the second harmonic conversion efficiency η_{SHG} reaches the maximum with increase in the photonic nanojet hotspot |E| and when its spatial profile is fully exterior to the core sphere but closest to the core and meta-shell interface, at which the $\chi^{(2)}$ nanostructures are at its highest density.

Comment 1: The FDTD simulation of the normalized SHG conversion efficiency, η_{SHG} (W^{-1}), shows that η_{SHG} is highest for the MSP having a PS or a SiO_2 core. This is an expected outcome

and can be predicted from the photonic nanojet features shown in **Section 3.3**. Here, the region of peak |E| in the nanojet hotspot is fully exterior to the core sphere, and at the same time, closest to the core interface at which the $\chi^{(2)}$ nanostructures are at its highest densities. With increasing n, the hotspots gradually internalize that leads to a decrease in the η_{SHG}. From $n > 2$, the photonic nanojet diminishes and hotspots are mostly confined within the core sphere and is accompanied by significant reduction in the η_{SHG}.

Comment 2: In calculating the conversion efficiency, we simplified the optical nonlinearities of ZnO NR to have isotropic susceptibility tensor having an effective $\chi^{(2)} = 15$ pm/V. The reference 13 reports a range of nonlinear coefficients from $d_{eff} = 2$ pm/V to 15 pm/V.[13,14] We have chosen a median value ($d_{eff} = 7.5$ pm/V) from the reported range to numerically approximate second harmonic conversion of the MSP.

Previous studies have shown that, despite considerably larger surface-to-volume ratio, the bulk property dominates over the surface effects in determining the $\chi^{(2)}$ of and the SHG by the ZnO 1D nanostructures.[15,16] In addition, previous studies have shown that $\chi^{(2)}$ values of 1D ZnO nanostructures,[13,14,16] such as nanorods and nanowires, are larger than that of ZnO in thin film[17] and bulk format (DAS et al., 2010). This is attributed to an increase in the permanent dipole moment when in the nanoscale 1D geometry. We believe the $\chi^{(2)}$ value used in the simulation is justifiable as we considered its range of experimental values obtained from ZnO nanorods/nanowires. Hence, the shape and size dependency of ZnO $\chi^{(2)}$ and its SHG is already take into account.

6. Experiment – Confocal Microscopy

6.1 SHG by MSP observed with confocal microscopy

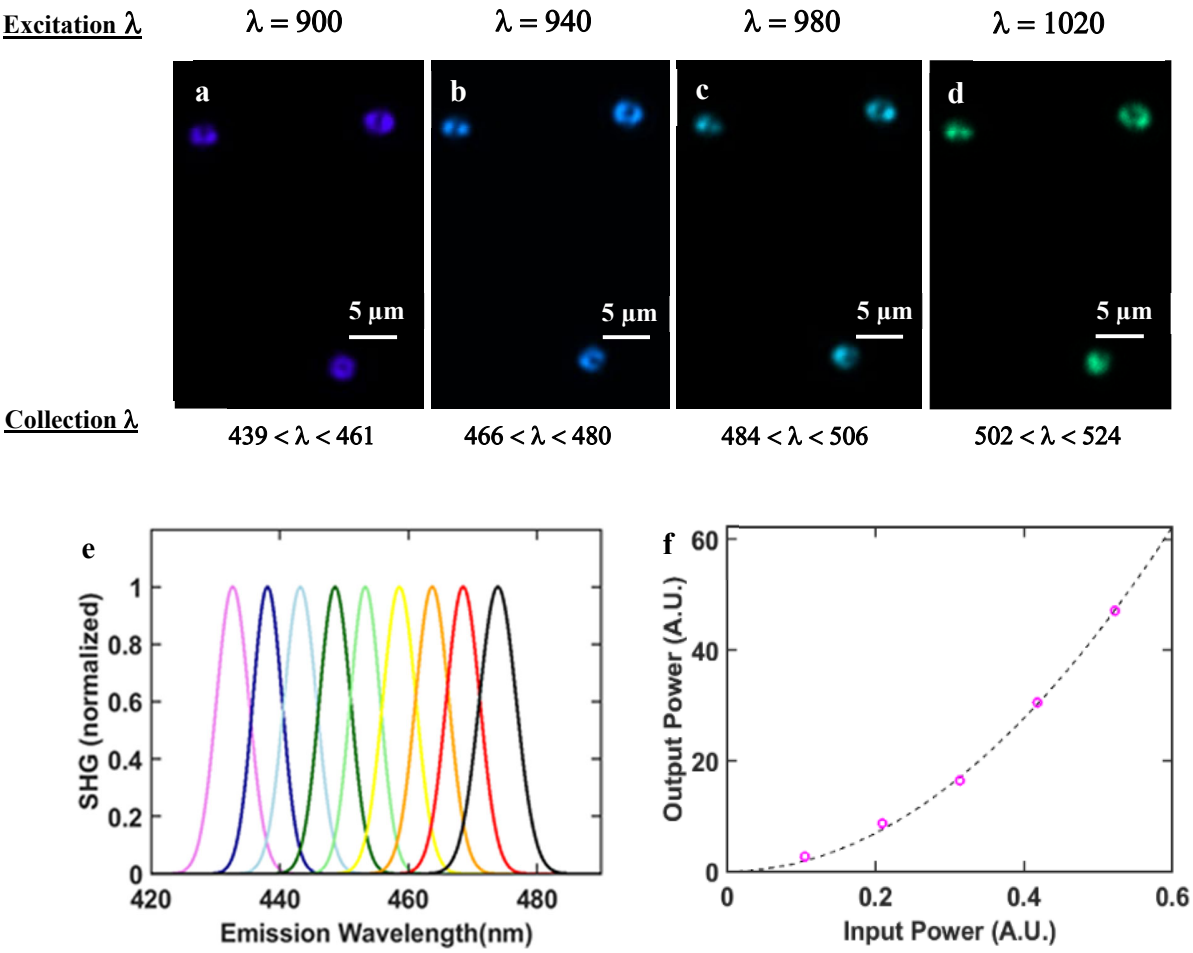

Figure S12. Second harmonic generation of light by the MSP. The MSP employed here are from **Figure 2d** in the main text, d_{core} = 1 µm, l = 600 nm, w = 120 nm (designated MSP 2.2). **a-f**, experimental observation confirming SHG of light by the MSP 2.2; images observed with confocal microscopy when excited with 2-photon laser at input wavelengths (**a**) λ = 900 nm, (**b**) λ = 940 nm, (**c**) λ = 980 nm, (**d**) λ = 1020 nm and collected at detector ranges of 439 nm < λ < 461 nm, 466 nm < λ < 480 nm, 484 nm < λ < 506 nm, 502 nm < λ < 524 nm, respectively, (**e**) spectral collection from the MSP2.2 upon irradiation at 860 nm < λ < 960 nm at 10 nm increments (the output intensity is normalized to scale between 0 and 1 independent of other wavelengths), (**f**) the SHG output intensities (I) (magenta, circle) demonstrates quadratic dependence to the input power (black, perforated, fit to $y = ax^2$, R-square: 0.9983);

Comment: Low numerical aperture objective (*NA* = 0.16) was utilized to ensure complete enclosure of MSP2.2 within the spot size (3.53 µm).

6.2 SHG is not detectable from individual/small aggregate of ZnO NRs at identical settings.

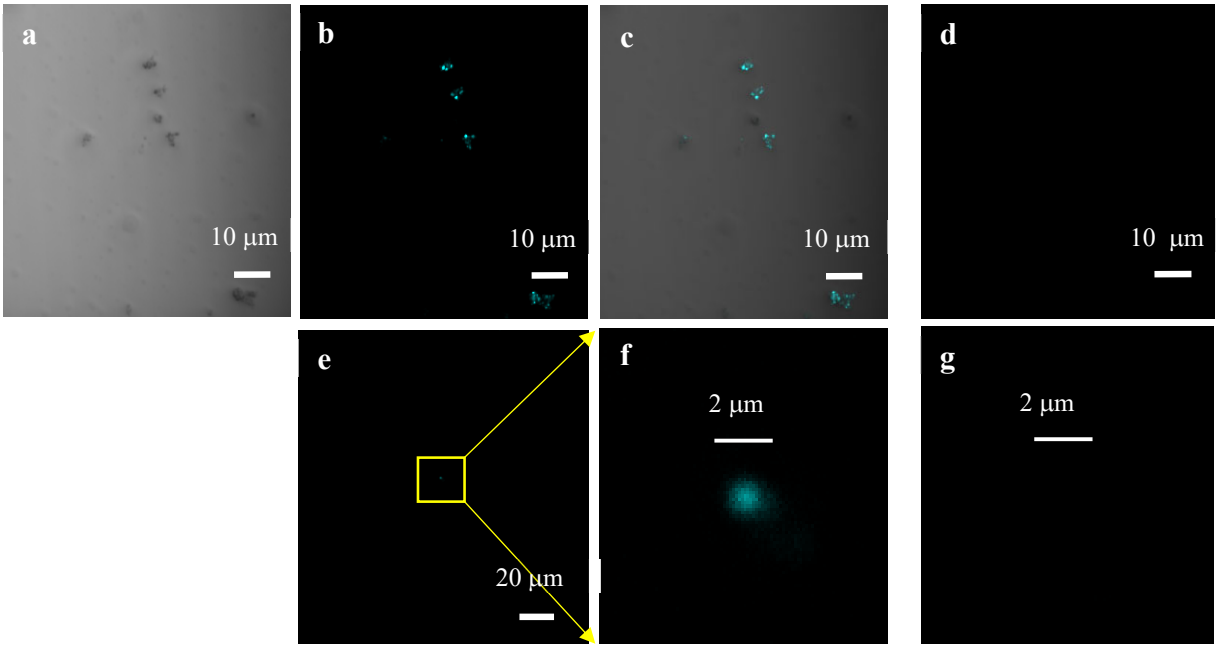

Figure S13. SHG by small aggregates of ZnO NRs. a-c, confocal microscopy images of small aggregates of ZnO NRs; (**a**) Transmission images of small aggregates of ZnO NRs, (**b**) The SHG images of small aggregates of ZnO NRs, irradiated at λ = 860 nm at maximum available power. The detectors are set to collect signals at 410 nm < λ_{output} < 464 nm. (**c**) the overlay of the SHG signals on the transmission image, (**d**) at identical imaging conditions that was utilized to characterize the SHG of the MSP2.2 (irradiated at 5% of the maximum available power through 5X objective), no visible signals were detected from the ZnO NR aggregates. A 50X objective was utilized to irradiate, collect and image the ZnO NRs in (**a-d**); **e-g,** confocal microscopy images of the SHG by the ZnO NRs that may be either a very small aggregate or an individual NR. The difference can not be distinguished due to diffraction limitations, (**e**) The SHG images obtained when irradiated with 2-photon laser at input wavelengths λ = 860 nm at maximum available power through a 100X objective. The signals are collected at 410 nm < λ_{output} < 464 nm, (**f**) 3X magnified image of (**e**), (**g**) At identical imaging conditions used for detecting and characterizing SHG from the MSP2.2, no visible signals were detected.

6.3 Expected enhancement in the conversion efficiency: MSP2.2 *vs.* ZnO NR

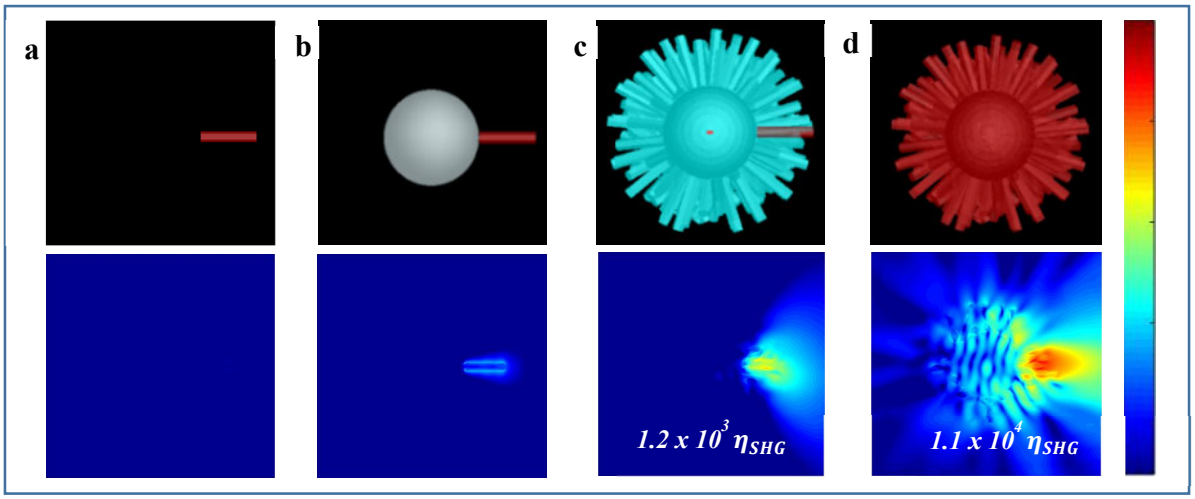

Figure S14. a-d, FDTD simulation demonstrating 4 orders of magnitude enhancement in the SHG conversion efficiency η_{SHG} between an MSP2.2 and a ZnO NR with pulsed input centered at λ = 900 nm. The heat map depicts |E| of the SHG generated by the MSP.

.

Comment 1: We also estimated the expected enhancement in the normalized conversion efficiency, η_{SHG}, from a ZnO NR to an MSP2.2 for a pulsed input centered at λ = 900 nm (τ = 100 fs), which depicts the confocal microscopy configuration used for initial characterization of the SHG by the MSP. When placing a single $\chi^{(2)}$ ZnO nanorod at the shadow side of a silica core, the photonic jet enhances its second harmonic η_{SHG} by an approximate 34 fold. In the presence of a meta-shell that features the effective optical responses, but without the $\chi^{(2)}$, there is additional 36-fold increase in the η_{SHG}. Finally, when 2nd order nonlinearity is assigned to the meta-shell in its entirety, as is the case with the MSP, there is an additional 9-fold increase in the η_{SHG}. Hence, there is a 4 order of magnitude enhancement in the η_{SHG} between a ZnO NR and their assemblies into an MSP.

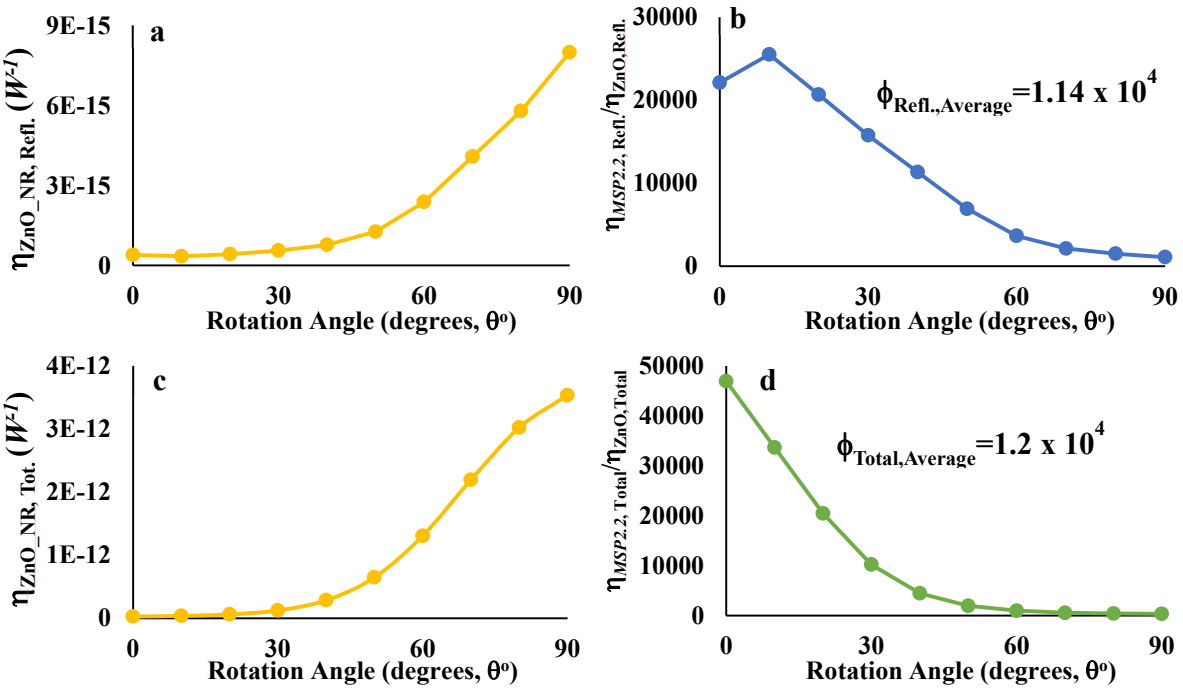

Figure S15. Full wave FDTD calculations of the SHG η_{SHG} of ZnO NRs and the model MSP2.2. The normalized conversion efficiency of ZnO NR (l = 600 nm, w = 120 nm) are calculated at 10^o increments in their orientations. The orientation of the ZnO NR is at 0^o when the polarization of the incident light is perpendicular to the ZnO NR *c*-axis, at 90^o when the polarization of the incident light is aligned with the ZnO NR c-axis. **a-b**, orientation dependent normalized conversion efficiency of ZnO calculated from the output collected in the *reflection monitor* in the simulation. The FDTD simulation emulates the confocal microscopy settings (NA = 0.16). (**a**) angle dependent normalized conversion efficiency for the ZnO NR, $\eta_{ZnO\text{-}NR,\ Refl.}$; (**b**) angle dependent enhancement in the normalized conversion efficiency by the model MSP2.2 from a single ZnO NR, $\phi_{Refl.} = \eta_{MSP2.2,\ Refl.}/\eta_{ZnO\text{-}NR,Refl.}$. The normalized conversion efficiency of the model MSP2.2 in the reflection monitor is $\eta_{MSP2.2,\ Refl.} = 8.72 \times 10^{-12}$ W^{-1}, and the conversion enhancement averaged over all angles is $\phi_{Refl.,Average} = \eta_{MSP2.2,\ Refl.,Average}/\eta_{ZnO\text{-}NR,Refl.,Average} = 1.11 \times 10^4$. **c-d**, FDTD simulation of orientation dependent normalized conversion efficiency calculated from the *total output* of the SHG; (**c**) angle dependent normalized conversion efficiency for the ZnO NR, $\eta_{ZnO\text{-}NR,Total.}$; (**d**) angle dependent enhancement in the normalized conversion efficiency by the model MSP2.2 from a ZnO NR, $\phi_{Total.} = \eta_{MSP2.2,\ Total.}/\eta_{ZnO\text{-}NR,Total}$. The normalized conversion efficiency of the model MSP2.2 calculated from the total SHG output is $\eta_{MSP2.2,\ Total} = 1.27 \times 10^{-9}$ W^{-1}, and the conversion enhancement averaged over all angles is $\phi_{Total,Average} = \eta_{MSP2.2,\ Total,Average}/\eta_{ZnO\text{-}NR,Total,Average} = 1.20 \times 10^4$. A TFSF pulse of τ = 100 fs centered at an arbitrary wavelength of λ = 896 nm was used as an input pump in the FDTD simulation that was applied to both the ZnO NRs and the MSP2.2.

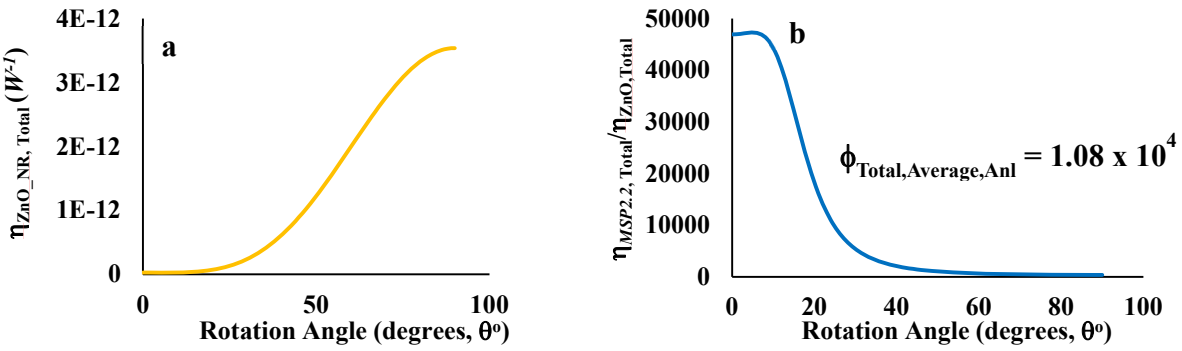

Figure S16. Analytical calculations of the SHG conversion efficiency for ZnO NRs and the model MSP2.2. Estimated enhancement in the normalized conversion efficiency by the MSP2.2 from a ZnO NR *via* analytical approach. (**a**) angle dependent normalized conversion efficiency for the ZnO NR, η_{ZnO_NR}; (**b**) angle dependent enhancement in the normalized conversion efficiency by the model MSP2.2 from a single ZnO NR, $\phi_{Total.} = \eta_{MSP2.2,\ Total.}/\eta_{ZnO,Total}$. The conversion enhancement averaged over all angles is $\phi_{Total,Average,Anl} = \eta_{MSP2.2,\ Total,Average}/\eta_{ZnO,Total,Average,Anl} = 1.08 \times 10^4$.

Comment: In this section, FDTD simulation is employed to estimate the enhancement in the normalized SHG conversion efficiency by the MSP2.2 ($\eta_{MSP2.2}$) from a single ZnO NR ($\eta_{ZnO\text{-}NR}$), $\phi = \eta_{MSP2.2}/\eta_{ZnO\text{-}NR}$.. The $\eta_{ZnO\text{-}NR}$ depends on its orientation relative to the polarization of the input pulse. The polarization of the input pulse is perpendicular to the ZnO NR *c*-axis at 0^o orientation and aligned at 90^o orientation. In the FDTD simulation that compares the conversion enhancement between the model MSP2.2 and a ZnO NR in the main text (**Figure 5c-f**) and **Figure S14,** only one orientation is considered. For a more comprehensive evaluation, the conversion enhancement (ϕ) is evaluated over 0° to 90° in the ZnO NR orientation, at 10° increments, and then averaged, $\phi_{Average} = \eta_{MSP2.2}/\eta_{ZnO\text{-}NR}$. The $\eta_{ZnO\text{-}NR}$ and $\phi_{Average}$ are computed *via* three approaches: 1) FDTD calculation of the enhancement in the normalized conversion efficiency taking into account only the reflected SHG output ($\phi_{Refl.,Average}$), **Figure S15a, b**. This FDTD setup emulates the confocal microscopy setting (NA = 0.16) employed in section **S6.1** and

S6.2, Figure S18; 2) FDTD simulation of the enhancement in the normalized conversion efficiency taking into account the total SHG output ($\phi_{Total,Average}$), **Figure S15c, d**; 3) analytical approach to estimate the enhancement in the conversion efficiency ($\phi_{Total,Average,Anl}$) based on the following expression, **Figure S16**:

$$P_{2\omega} = \eta(\theta) \times P_{\omega}^{2}$$

$$\eta(\theta) = \eta_x P_{\omega}^{2} cos^{4}\theta + \eta_y P_{\omega}^{2} sin^{4}\theta$$

, where η_x and η_y are the normalized conversion efficiency of ZnO NR at 0° and 90° orientation respectively and are obtained from the FDTD simulations.

Due to spherical configuration, the normalized SHG conversion efficiency of the model MSP2.2, $\eta_{MSP2.2}$, are assumed orientation independent and are therefore evaluated at only one incident angle. The enhancement in the conversion efficiency by the MSP2.2 from a single ZnO NR averaged over a quadrant of angles are equivalent in all the three approaches considered; $\phi_{Refl.,Average}$ = 1.14 x 10^4, $\phi_{Total,Average}$ = 1.2 x 10^4, $\phi_{Total,Average,Anl}$ = 1.08 x 10^4.

6.4 Comparison of SHG conversion efficiency between MSP of different meta-shell thickness

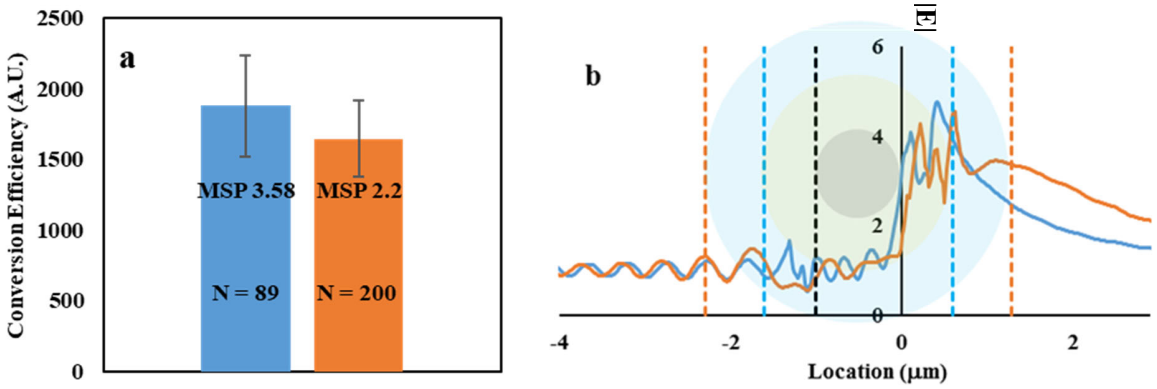

Figure S17. Normalized conversion efficiency comparison between MSP2.2 and MSP3.58. The MSP3.58 consists of SiO_2 core sphere (d = 1 μm) with meta-shell of thickness 1.29 μm (ZnO NR l = 1290 nm, w = 120). (**a**) SHG conversion efficiency, in arbitration units, obtained for the MSP3.58 (N = 89) and the MSP2.2 (N = 200). (**b**) FDTD simulation shows that the peak |E| at the photonic nanojet hotspot in the MSP3.58 and in the MSP2.2 are comparable. The blue and the orange line represents the |E| for MSP3.58 and MSP2.2, respectively.

Comment 1: The MSP3.58 consists of SiO_2 core sphere (d = 1 μm) with a meta-shell thickness of 1.29 μm (ZnO NR l = 1290 nm, w = 120). Interestingly, the normalized SHG conversion efficiency for the MSP3.58 ($\eta_{MSP3.58}$) and that of MSP2.2 ($\eta_{MSP2.2}$) are comparable ($^{\eta_{MSP3.58}}/_{\eta_{MSP2.2}} = 1.38$). This is due to comparable peak electric field |E| in the nanojet hotspot for the both types. The measurement was carried out with confocal microscopy in which the MSP are irradiated with femtosecond pulses (140fs, 80MHz) centered at λ = 900 nm and at 5% of its maximum available power. The images are collected at 439 nm < λ_{output} < 461 nm. In order to fully immerse the MSP within the spotsize, a low NA (0.16) 5X objective was use. The SHG intensities obtained from the images are subtracted by the background noise, normalized by the gain settings, followed by normalization with the square of the input power reading.

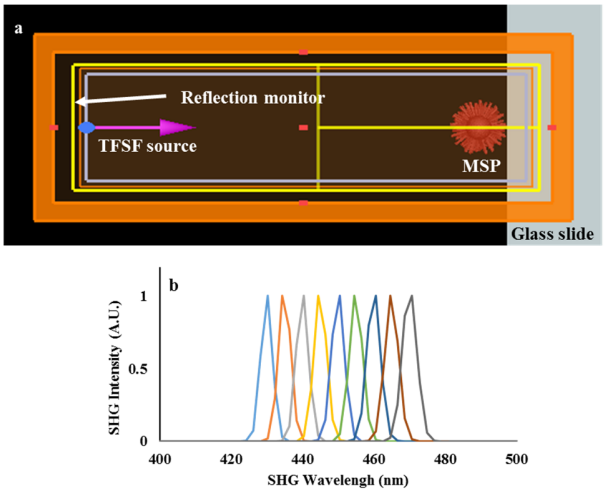

Figure S18. (**a**) FDTD simulation setup, *NA* = 0.16; (**b**) FDTD simulations of the SHG output from the MSP2.2 irradiated at different wavelengths ranging from 860 nm to 940 nm.

Comment 2: The geometry of the reflection monitor and its distance from the particle, in the FDTD simulation setup, is arranged to emulate the numerical aperture *NA* (0.16) of the objective employed in the confocal microscopy measurement, **Figure S18**. TFSF sources are employed as the input pulse centered at λ_{input} = 900 nm with pulse length τ = 100 fs. A glass slide is placed behind the model MSP2.2 to recapture the experimental setting. The ZnO NRs are imparted with 2nd order nonlinear susceptibility $\chi^{(2)}_{eff}$ = 15 pm/V.

Comment 3: The FDTD simulation is carried out to estimate and compare the normalized conversion efficiency of the MSP.358 and MSP2.2. In accordance with the experimental setting, only the SHG output collected in the reflection monitor (NA = 0.16) is taken into account in the calculation, as in **comment 1**. The FDTD simulation also results in a similar normalized conversion efficiency between the MSP3.58 and the MSP2.2. While the total conversion efficiency for the MSP3.58 is $\eta_{\mathrm{MSP3.58\_FDTD\_tot}} = 1.87 * 10^{-9}\ \mathrm{W}^{-1}$, the conversion efficiency

evaluated with the reflected SHG is $\eta_{\mathrm{MSP3.58\_FDTD\_refl}} = 8.81 * 10^{-12}\ \mathrm{W}^{-1}$. In the case of MSP2.2, while the total conversion efficiency is $\eta_{\mathrm{MSP3.58\_FDTD\_tot}} = 1.23 * 10^{-9}\ \mathrm{W}^{-1}$, the conversion efficiency evaluated with the reflected SHG is $\eta_{\mathrm{MSP3.58\_FDTD\_refl}} = 7.15 * 10^{-12}\ \mathrm{W}^{-1}$. Hence, the ratio of the conversion efficiency taking into account only the reflected SHG, as in the experimental setting, $\eta_{\mathrm{MSP3.58\_FDTD\_refl}} / \eta_{\mathrm{MSP2.2\_FDTD\_refl}} = 1.23$, which closely approximates the experimental findings.

6.5 Comparison of SHG conversion efficiency of MSP2.2 having SiO_2 core and TiO2 core.

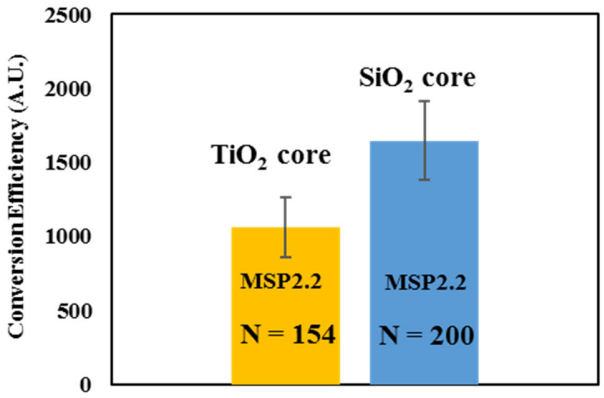

Figure S19. Normalized conversion efficiency comparison between MSP2.2 having a SiO_2 core and a TiO_2 core. Confocal microscopy is used to evaluate and compare the conversion efficiency between the two MSP2.2 types. See **Section 6.4**, **Comment 1** for the experimental measurement setting.

Comment: The SHG conversion efficiency by two MSP2.2 types, one having a SiO_2 core and one having a TiO_2 core are compared.

Due to the high refractive index of TiO_2 (n = 2.5 at λ = 900 nm) the photonic nanojet at the shadow side disappears and the hotspots are dispersed within and along the interface of the core sphere, as seen in the FDTD simulations in section **3.3**, **Figure S8**. This results in a lack of spatial overlap between the |E| hotspot and the $\chi^{(2)}$ nanostructures. Hence, reduction in the SHG conversion efficiency for the MSP2.2 with the TiO_2 core is expected. Such is observed through experimental measurement *via* confocal microscopy. The conversion efficiency ratio between MSP2.2 of TiO_2 and of SiO_2 core from the measurement is $\eta_{\mathrm{MSP2.2\_TiO2\_exp}}/\eta_{\mathrm{MSP2.2\_SiO2\_exp}} = 0.64$. The experimental setup is identical to that employed in section **6.1 – 6.4**. The FDTD simulation also results in a similar observation. While the total conversion efficiency for the MSP2.2 with TiO2 core is $\eta_{\mathrm{MSP2.2\_TiO2\_FDTD\_tot}} = 4.7 * 10^{-10}\ \mathrm{W}^{-1}$, the conversion efficiency evaluated from the reflected SHG is $\eta_{\mathrm{MSP2.2\_TiO2\_FDTD\_refl}} = 4.1 * 10^{-12}\ \mathrm{W}^{-1}$. The ratio of the conversion efficiency taking only the reflected SHG into consideration is $\eta_{\mathrm{MSP2.2\_TiO2\_FDTD\_refl}}/\eta_{\mathrm{MSP2.2\_SiO2\_FDTD\_refl}} = 0.57$, which closely approximates the experimental findings.

7 Experiment – Nonlinear optical microscopy

7.1 Schematics – NLO microscopy

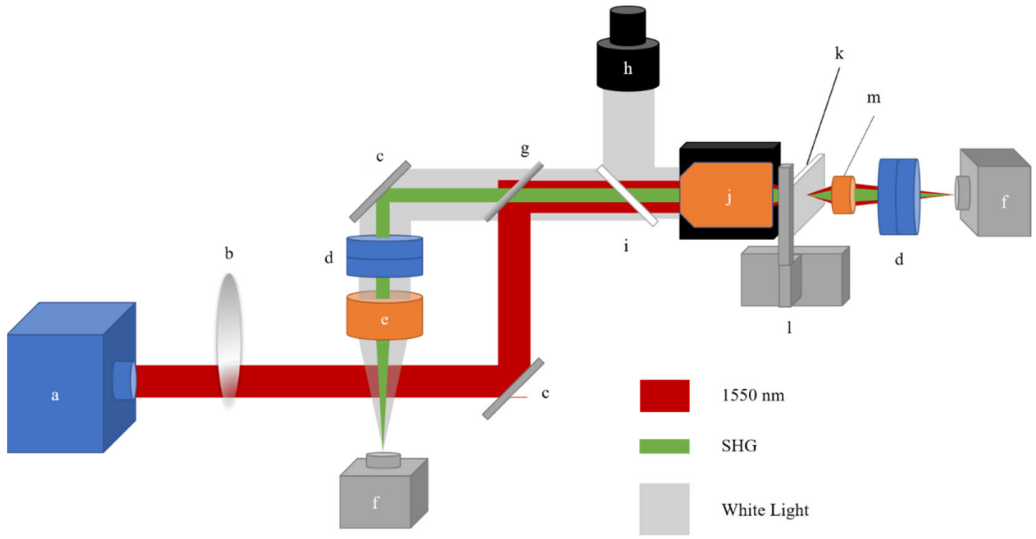

Figure S20. Schematic of the NLO microscopy setup used to measure the SHG generated by the MSP.

Comment: The schematic in **Figure S20** depicts the nonlinear optical (NLO) microscopy setup constructed to detect the SHG generated by the MSP. **Table S1** shows the optical components employed in the setup. Ultra-short pulse frequency comb (Menlo Systems, τ = 80 fs , f_{rep} = 250 MHz) centered at λ_{in} = 1550 nm is used as the input source. The input pulse is subject to a continuously variable neutral density filter wheel to obtain variable input average power. The input beam is guided into a 50x objective (Mitutoyo Plan APO NIR, *NA* = 0.42) and focused onto a single particle on the sample slide with a spot size $d_f \approx$ 2.6 μm. A collimated LED white light source was incorporated to locate and focus the input pulse into individual MSP. The backscattered SHG is subject to a pair of filters to remove the input light and the third harmonic generation. A 1" VIS lens was used to focus the SHG onto a photodiode power sensor. The total average power of the backscattered SHG is then determined by accounting for the power loss

through each optical component. The transmission values of each optical component that the SHG passes through are shown in **Table S2**.

The forward scattered SHG was collected *via* aspheric condenser lens *(NA* .79, F = 16 mm) and subject to a pair of filters to remove the input pump and the higher order harmonic generations identical to the reflection mode setup. The total average power of the forward scattered SHG is then determined by accounting for the power loss through each optical component, listed in **Table S2**. The aspheric condenser lens was replaced with a 60X objective (Nikon, M Plan 60, 630770) when taking the forward scattered images to obtain the farfield pattern.

a	Frequency comb centered at 1550 nm, 80fs, 250 MHz
b	Round continuously variable ND filter wheel
c	Silver mirrors
d	Filters to remove pump and higher order harmonic wavelengths
e	VIS lens
f	Camera/780 nm/ detector
g	Shortpass dichroic mirror
h	Collimated LED white light source
i	VIS beam splitter
j	50x Objective
k	Sample slide coated with meta-shell supraparticles
l	x, y-stage
m	Aspheric condenser lens / 60 X objective

Table S1: List of labeled components in **Figure S20**

Optical Component	Percent Transmission (%)	
50x Mitutoyo Plan APO NIR, NA = 0.42	67 (**Supplementary Information section 7.2)**	Emperical
Thorlabs DMSP950	97.6979	Thorlabs Raw Data
Thorlabs FESH0800	98.201267	Thorlabs Raw Data
Thorlabs FELH0550	94.94641	Thorlabs Raw Data
Thorlabs VIS (A-coating) lenses	96.56032	Thorlabs Raw Data

Table S2: Percent transmission values for various optical components in the experimental setup that were used to determine the total average SHG power generated. The values are for light of wavelength λ = 780 nm.

7.2 Schematics – Objective calibration

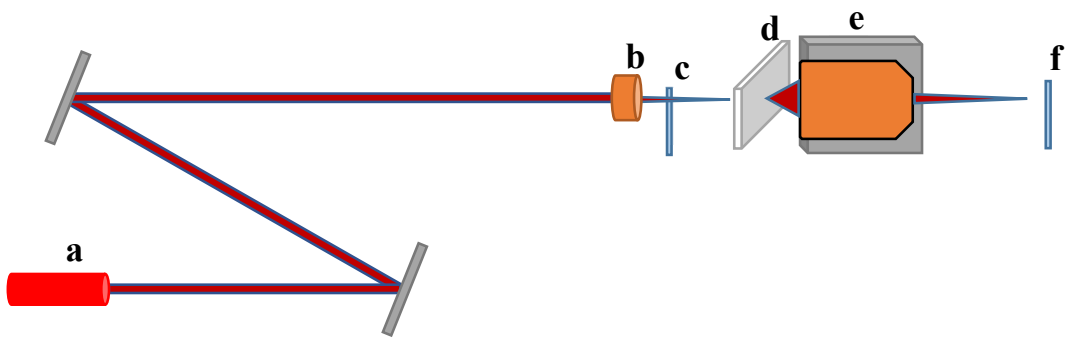

Figure S21. Schematic for the objective calibration setup

a	Laser diode, λ = 775 nm
b	Lens, *f* = 15 mm
c	Power detector
d	Glass slide
e	Objective to be calibrated
f	Power detector

Table S3: List of labeled components in **Figure S21**

7.3 Calibration - Average input power delivered to the sample

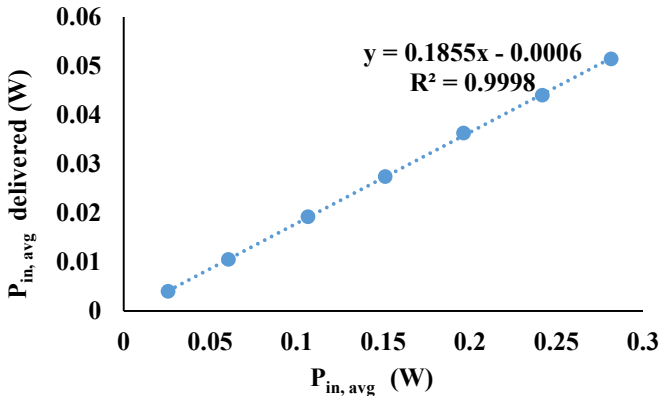

Figure S22. Calibration curve for the average input power, $P_{in,avg}$, delivered to the sample.

Comment: The calibration curve for the average input power delivered to the sample is obtained from the power reading of the input source recorded prior to the continuously variable neutral density filter wheel and that immediately after the objective. Thermal power sensor head (Thorlabs) is utilized for the measurement.

7.4 FDTD - Simulation setup to replicate NLO microscopy setting

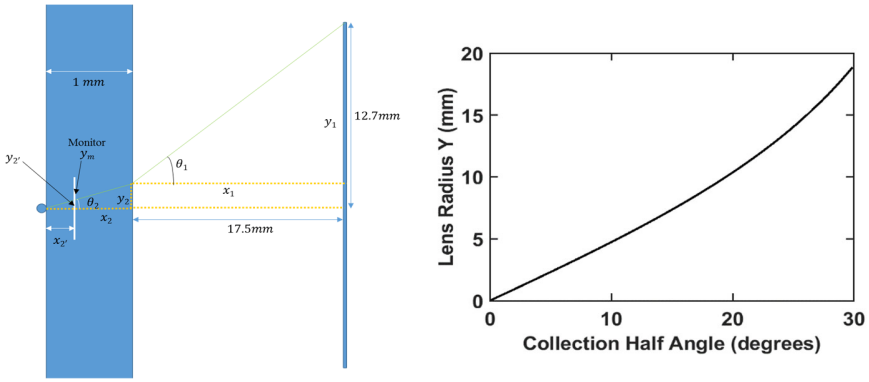

Figure S23. Schematic for the objective calibration setup

Comment 1: TFSF sources are employed as the input pulse centered at λ_{input} = 1550 nm with pulse length τ = 80 fs. A glass slide is placed behind the model MSP2.2 to recapture the experimental setting. The ZnO NRs are imparted with 2nd order nonlinear susceptibility $\chi^{(2)}_{eff}$ = 15 pm/V.

Comment2: The power monitor in the FDTD simulation is set up to mirror the half collection angle devised in the experimental setup. Taking n = 1.5 for the glass slide, the following relationship is satisfied

$$Y = y1 + y2 = \tan(\theta 2) + 17.5 * \tan(\theta 1)$$

$$= \tan(\theta 2) + 17.5 * \tan(Sin^{-1}(1.5 * sin(\theta 2)) < 12.7 \text{ mm}$$

, where Y is radius of the lens. From the relationship, the maximum half angle of collection for the transmission measurement of the SHG signal, using an aspherical condenser lens (d = 25.4 mm, NA = 0.8), is approximately 23°. The half collection angle for the reflection measurement is approximately 25°.

7.5 FDTD - Normalized Conversion Efficiency

FDTD simulation is set up to emulate the experimental settings in the NLO microscopy (**Section 7.4**). From the FDTD calculations, the normalized SHG conversion efficiency by the MSP2.2, where the simulation takes into account only the reflected SHG captured by the objective used in the experiment, is $\eta_{MSP2.2, Refl.} = 8.53 \times 10^{-12}$ W^{-1}. Taking into account only the forward scattered SHG captured by the aspheric condenser lens, the normalized SHG conversion efficiency by the MSP2.2 is $\eta_{MSP2.2, forward} = 6.8 \times 10^{-11}$ W^{-1}. These values are close to the experimental results observed from the custom built NLO microscopy. The normalized conversion efficiency for the total SHG generated by the MSP2.2 is $\eta_{MSP2.2, Total} = 1.48 \times 10^{-10}$ W^{-1}.

7.6 Farfield Radiation Pattern (Reflection) and quadratic dependence to input power

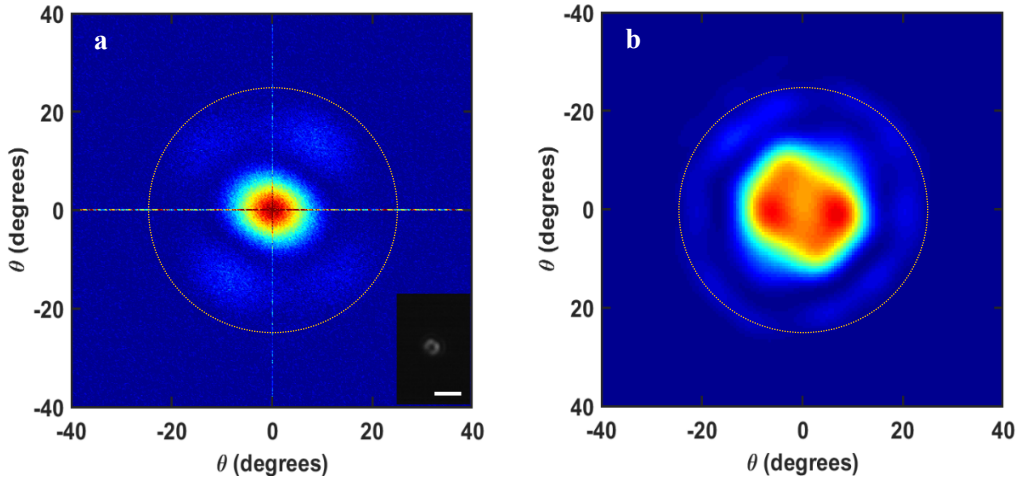

Figure S24. Farfield radiation pattern of the reflected SHG. (**a**) Far field radiation pattern of the reflected SHG (inset: image of the reflected SHG), (**b**) FDTD simulation of the far field radiation pattern of the reflected SHG. Dotted circle represents the angle of collection for the objective (*NA* 0.42) utilized in the imaging setup. scale bar: 5 μm

Comment 1: For imaging reflected SHG, the half angle of collection for the objective used in the setup is $\theta = 24.83^o \approx 25^o$. For imaging the forward scattered SHG, we replaced the aspheric condenser lens with the 60X objective (**Section 7.1**), increasing the half angle of collection to approximately $\theta = 27.81^o \approx 28^o$.

Comment 2: The far field radiation pattern is obtained by taking FFT of the SHG image in which the background noise is subtracted.

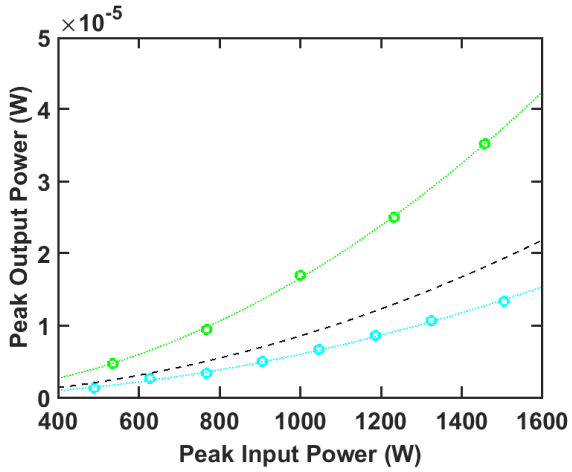

Figure S25. SHG output power display quadratic dependence to the input power. The samples displaying an upper limit (green circle) and a lower limit (cyan circle) in the conversion efficiency values are plotted. The dotted green line (R = 0.996, $\eta = 1.657 \times 10^{-11}$) and the dotted cyan line (R = 0.9997, $\eta = 5.995 \times 10^{-11}$) are the respective curve fit ($y = \eta x^2$) to the quadratic relationship. The quadratic relationship calculated from the FDTD simulation (black perforated line, $\eta = 8.53 \times 10^{-12}$) fall within the experimental range.

8 Additional analytical calculations

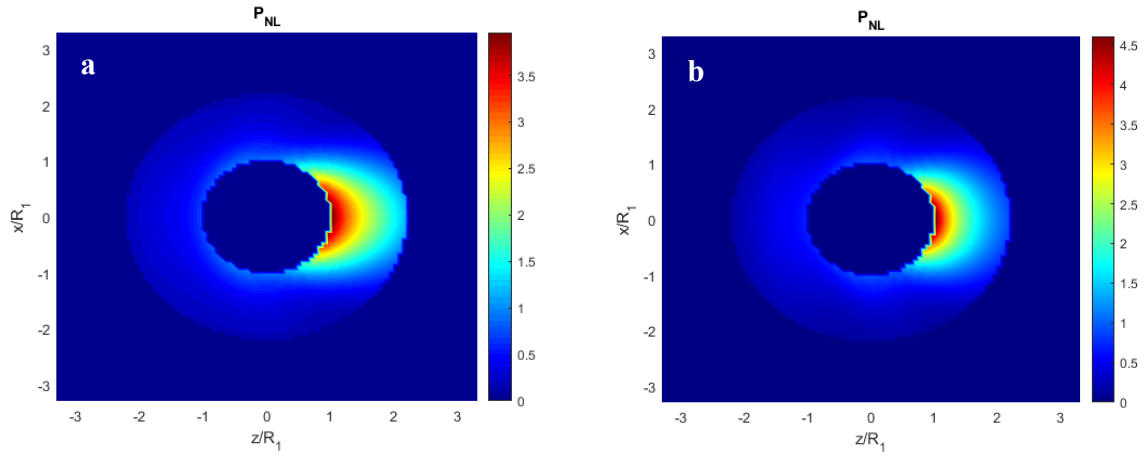

Fig. S26. Nonlinear second-harmonic polarization for the configurations shown in Figs. 4l (**a**) and 4k (**b**). It is seen that while the field intensity is stronger for the isotropic case (**Fig. 4l**), the nonlinear polarization peak is higher for the anisotropic case (**Fig. 4k**) because the radial anisotropy can engineer the location of the hot spot to spatially overlap with the volume having the highest densities of $\chi^{(2)}$ nanostructures. A volume integral of the nonlinear polarization for this case shows that the difference is less than 5%. Note that if the nanowires are oriented randomly (realistic case for isotropic shell), the average permittivity of both configurations will be the same. Hence, the effect of anisotropy on enhanced nonlinear response would be more pronounced, permittivity of both configurations will be the same. Hence, the effect of anisotropy on enhanced nonlinear response would be more pronounced.

9. Reference

1. Montjoy, D.G.; Bahng, J.H.; Eskafi, A.; Hou, H.; Jiang, R.; Kotov, N.A. Photocatalytic Hedgehog Particles for High Ionic Strength Environment: Electric Field Catalysis without Electrodes. *Publ. pending*.

2. Glas, F. Critical Dimensions for the Plastic Relaxation of Strained Axial Heterostructures in Free-Standing Nanowires. *Phys. Rev. B* **2006**, 74, 121302.

3. Ertekin, E.; Greaney, P. A.; Chrzan, D. C.; Sands, T. D. Equilibrium Limits of Coherency in Strained Nanowire Heterostructures. *J. Appl. Phys.* **2005**, 97, 114325.

4. Peterson, R. B.; Fields, C. L.; Gregg, B. A. Epitaxial Chemical Deposition of ZnO Nanocolumns from NaOH Solutions. *Langmuir* **2004**, 20, 5114–5118.

5. Miroshnichenko, A. E.; Kivshar, Y. S. Fano Resonances in All-Dielectric Oligomers. *Nano Lett.* **2012**, 12, 6459–6463.

6. Kuznetsov, A. I.; Miroshnichenko, A. E.; Brongersma, M. L.; Kivshar, Y. S.; Luk'yanchuk, B. Optically Resonant Dielectric Nanostructures. *Science (80-.).* **2016**, 354, aag2472.

7. Luk'yanchuk, B. S.; Paniagua-Domínguez, R.; Minin, I.; Minin, O.; Wang, Z. Refractive Index Less than Two: Photonic Nanojets Yesterday, Today and Tomorrow [Invited]. *Opt. Mater. Express* **2017**, 7, 1820.

8. Chen, Z.; Taflove, A.; Backman, V. Photonic Nanojet Enhancement of Backscattering of Light by Nanoparticles: a Potential Novel Visible-Light Ultramicroscopy Technique. *Opt. Express* **2004**, 12, 1214–1220.

9. Garnett, J. C. M. XII. Colours in Metal Glasses and in Metallic Films. *Philos. Trans. R. Soc. London A Math. Phys. Eng. Sci.* **1904**, 203, 385–420.

10. Niklasson, G. A.; Granqvist, C. G.; Hunderi, O. Effective Medium Models for the Optical Properties of Inhomogeneous Materials. *Appl. Opt.* **1981**, 20, 26–30.

11. Jahani, S.; Jacob, Z. Transparent Sub-Diffraction Optics: Nanoscale Light Confinement without Metal. *2014 IEEE Photonics Conf. IPC* **2014**, 1, 581–582.

12. Qiu, C.W.; Luk'yanchuk, B. Peculiarities in Light Scattering by Spherical Particles with Radial Anisotropy. *J. Opt. Soc. Am. A* **2008**, 25, 1623–1628.

13. Das, S. K.; Bock, M.; O'Neill, C.; Grunwald, R.; Lee, K.M.; Lee, H.W.; Lee, S.; Rotermund, F. Efficient Second Harmonic Generation in ZnO Nanorod Arrays with Broadband Ultrashort Pulses. *Appl. Phys. Lett.* **2008**, 93, 181112.

14. Dhara, S.; Lynch, S.A. Chapter 2, Second Harmonic Generation in ZnO Nanowires. *Nanowires - New Insights*. IntechOpen. **2017**. Open access peer-reviewed Edited Volume

15. Larciprete, M. C.; Centini, M. Second Harmonic Generation from ZnO Films and Nanostructures. *Appl. Phys. Rev.* **2015**, 2, 31302.

16. Das, M.; Rana, S.; Sen, P. Second Harmonic Generation in ZnO Nanorods. *J. Nonlinear Opt. Phys. Mater.* **2010**, 19, 445–458.

17. Narayanan, V.; Thareja, R. K. Harmonic Generation in ZnO Nanocrystalline Laser Deposited Thin Films. *Opt. Commun.* **2006**, 260, 170–174.